frontiers in Earth Science

ORIGINAL RESEARCH
published: 27 November 2018
doi: 10.3389/feart.2018.00202

A Paleomagnetic Inspection of the Paleocene-Eocene Thermal Maximum (PETM) in the Southern Pyrenees

Belén Oliva-Urcia[1,2]*, *Inmaculada Gil-Peña*[3], *José M. Samsó*[4], *Ruth Soto*[5] and *Idoia Rosales*[6]

[1] Department of Geology and Geochemistry, Sciences Faculty, Universidad Autonoma de Madrid, Madrid, Spain, [2] Departamento de Ciencias de la Tierra, Universidad Zaragoza, Zaragoza, Spain, [3] Instituto Geológico y Minero de España, Madrid, Spain, [4] Consulting Geologist, Jaca, Spain, [5] Instituto Geológico y Minero de España, Unidad de Zaragoza, Zaragoza, Spain, [6] Instituto Geológico y Minero de España, Madrid, Spain

Magnetic properties of rocks can be useful for determining paleoenvironmental changes. A dramatic climate change that occurred in the Paleocene-Eocene Thermal Maximum (PETM) modified the environment and, hence, the magnetic properties recorded in the sediments. New paleomagnetic data from marine records of the PETM in the Southern Pyrenean zone displays a variation of the magnetic parameters in four different sections. The magnetic signal reveals a positive excursion of magnetic values starting before the onset of the marly interval of La Faja de las Flores Mb (beginning of the PETM record, Ilerdian) in the Carriata section with a maximum value in the marly interval. A similar magnetic signal is observed in the Bujaruelo section (~10 km south of Carriata at PETM times) that is related directly to the marly interval of Faja de las Flores Mb. However, towards the south, the PETM interval does not appear in the sedimentary record; therefore, in the southern Gallisué section, no magnetic excursion occurs. In the southernmost-studied Entremón section, a positive magnetic excursion occurs in a thin marly interval unrelated to the PETM, and in two lower intervals of the column. All sections were later subjected to deformation during the pyrean orogeny and the three northernmost sections in the regional cleavage front, where pressure solution and remagnetizations have been described. A post-folding remagnetization component is found in the three northern sections.

Keywords: paleomagnetism, magnetic signal, magnetic minerals, Pyrenees, remagnetization

OPEN ACCESS

Edited by:
Luigi Jovane,
Universidade de São Paulo, Brazil

Reviewed by:
Daniel J. Peppe,
Baylor University, United States
Simone Sonvesso Mantovanelli,
Universidad de São Paulo, Brazil

***Correspondence:**
Belén Oliva-Urcia
belen.oliva@uam.es

Specialty section:
This article was submitted to Geomagnetism and Paleomagnetism, a section of the journal Frontiers in Earth Science

Received: *29 June 2018*
Accepted: *26 October 2018*
Published: *27 November 2018*

Citation:
Oliva-Urcia B, Gil-Peña I, Samsó JM, Soto R and Rosales I (2018) A Paleomagnetic Inspection of the Paleocene-Eocene Thermal Maximum (PETM) in the Southern Pyrenees. Front. Earth Sci. 6:202. doi: 10.3389/feart.2018.00202

INTRODUCTION

The Paleocene-Eocene Thermal Maximum (PETM) has drawn the attention of investigators on global change over the last decades as it represents a good ~56 Ma ago analog to the present-day dramatic warming related to massive carbon release into the ocean-atmosphere system (Kennett and Stott, 1991; Dickens, 1999; Norris and Röhl, 1999; Bowen et al., 2006; McInerney and Wing, 2011). The PETM involved a rapid increase of 4–10°C of the Earth's surface temperature (Zachos et al., 2008), and it is associated with the sedimentary record with a negative $\delta^{13}C$ excursion in both marine and terrestrial organic matter and carbonate as a result of the massive influx of the light carbon isotope (Kennett and Stott, 1991; Koch et al., 1992; Luterbacher et al., 2000).

A subtle excursion in $\delta^{13}C$ and $\delta^{18}O$ has been found to the east and west of the studied area (Pujalte et al., 2003, 2009); however, no clear data from stable isotopes have been published yet (Pujalte et al., 2016). Nevertheless, unpublished data from stable isotopes in the Carriata section show the PETM excursion, particularly for $\delta^{18}O$ (Rosales et al., in prep.).

The importance of the PETM lies in its major ecological consequences. In the oceans, deep-sea benthic foraminifera experienced their greatest extinction during the last 75 Million years (Thomas, 1990; Thomas and Shackleton, 1996), planktonic foraminifera, and calcareous nannoplankton experienced transient diversifications at the onset of the PETM (Kelly et al., 1996; Gibbs et al., 2006), and the correlation of the PETM with a major larger foraminifera turnover (LFT), between SBZ4 and SBZ5 (shallow benthic zones; Serra-Kiel et al., 1998), characterized by the first appearance of lenticular nummulites and true Alveolina is widely acknowledged (Orue-Etxebarria et al., 2001; Pujalte et al., 2003, 2009; Scheibner et al., 2005; Scheibner and Speijer, 2009; Zamagni et al., 2012; Drobne et al., 2014). On land, archaic mammals were replaced by modern groups (Clyde and Gingerich, 1998; Bowen et al., 2002; Gingerich, 2003; Wing et al., 2005; Secord et al., 2012) and the floras experienced important changes (Jaramillo et al., 2006).

The record of the PETM, its duration, cause(s), and effects have been analyzed around the world using different methodologies (paleontological, sedimentological, and geochemical). The duration of the PETM has been investigated mainly to quantify the mass of carbon released to deduce the origin of the light carbon released into the atmosphere. The effort to quantify the duration with orbitally tuned sections is discussed in Röhl et al. (2003, 2007), Aziz et al. (2008), and Charles et al. (2011) and using extraterrestrial ^{3}He fluxes in Farley and Eltgroth (2003) and Murphy et al. (2010). The onset of PETM has been analyzed with extracted marine sediments because of the Ocean Drilling Program (IODP now) and on inland sections (marine and terrestrial rocks) (McInerney and Wing, 2011 and references therein). In sea sediments, the onset of PETM coincides with the sharp and negative carbonate isotopic excursion (CIE) on clays (core layer) due to decalcification after the massive carbonate dissolution (Röhl et al., 2007). These authors suggest that the total duration of the PETM is 170 kyr, as the duration of the core layer is 5 precession cycles and the duration of the recovery of the carbon isotopic excursion until the carbon isotope values return to background value is about 3.5 precession cycles. Other studies suggest that the PETM spans up to 236 kyr (Charles et al., 2011), whereas McInerney and Wing (2011) estimate the duration of the PETM to be between 170 and 220 kyr (8–23 kyr correspond to the onset event, 115 kyr to the core event, and 50–85 kyr to the recovery event). In terrestrial sediments of the Bighorn Basin (USA), the beginning of the PETM is characterized by two distinct release events of carbon, separated by a recovery to background values, with a rate of carbon release more similar to present-day anthropogenic emissions (Bowen et al., 2015 and references therein). Models of heat transfer in marine sediments explain the long duration of the PETM suggest a slow and long-lasting release of light carbon due to a bottom water temperature anomaly (Zeebe, 2013).

Different hypotheses have been proposed to link the injection of light carbon to the warming PETM event (see references in Kopp et al., 2009). An accelerated hydrogeological cycle is one of the effects of the warming event that determines changes in the sedimentation pattern in continental margins (USA) (Gibson et al., 2000; Villasante-Marcos et al., 2009 and references therein) and in fluvial environments (Colorado, USA; Foreman et al., 2012) or extreme precipitations from megafan in a braid plane in the Pyrenees (Schmitz and Pujalte, 2007). This change in the sedimentation pattern is reported from more intense chemical weathering on the continents and an increased siliciclastic input on marine environments due to an acceleration of the hydrological and weathering cycles (e.g., Kelly et al., 2005; Dickens, 2008; Pujalte et al., 2016) together with a drop in redox conditions (Villasante-Marcos et al., 2009).

Regarding the rock magnetic properties/magnetic properties of rocks, an early controversy emerged from the North Atlantic continental margin in terms of the origin of the magnetic minerals found at the PETM. At first, some authors favored a comet impact (Kent et al., 2003; Cramer and Kent, 2005), but, later on, a biogenic origin of the magnetic minerals (magnetotactic bacteria) explained the special magnetic properties (Lippert et al., 2004; Kopp et al., 2007; Lippert and Zachos, 2007). Villasante-Marcos et al. (2009) analyzed the paleomagnetic signal of uplifted sections of the marine upper slope to an outer shelf in New Zealand, where the biogenic origin of the magnetic properties of the PETM was not found. However, the determination of the magnetic properties of such an interval (Dee Marls Fm) suggests an increase in the terrigenous supply.

Another characteristic of the PETM and the Earth's magnetic field is that a short-lived reversal of the magnetic field during the PETM was found in an ocean drill core that was related to other paleomagnetic records of continental rocks in the Bighorn Basin and in ocean drill cores in the southern and northern Atlantic (Lee and Kodama, 2009 and references therein). Notwithsanding a possible anomaly in the paleomagnetic record, these authors suggest a possible coupling between Earth's core magnetofluid dynamo sphere and the atmosphere-hydrosphere during an abrupt catastrophic climate event.

The goal of this paper is to provide new classical paleomagnetic data from shallow platform marine sediments of the PETM interval in the Southern Pyrenees. The PETM sediments underwent the deformation processes and the cleavage developments during the alpine deformation. The discussion focused on the magnetic signal and the effects of the deformation on the primary magnetic mineralogy was affected by the hydrological and redox changes during the PETM.

GEOLOGICAL SETTING

This work is based on stratigraphic observations and magnetic analysis of four sections located in the Southern Pyrenees: Carriata and Bujaruelo sections in the North, Gallisué to the South, and Entremón is the southernmost section (**Figure 1A**).

All sections were deposited in and/or near a shallow marine platform environment in the southern side of the E-W marine

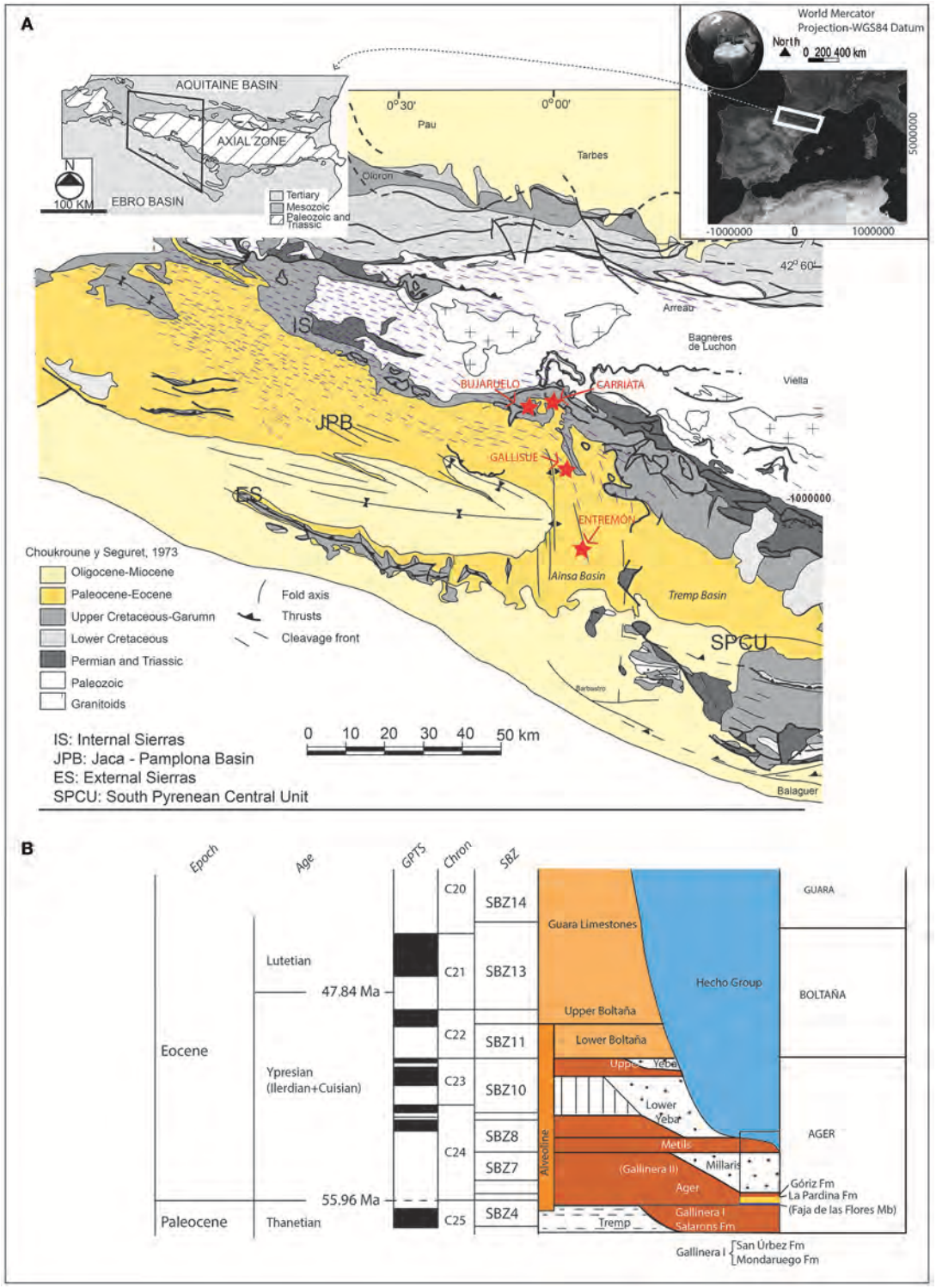

FIGURE 1 | (A) Present-day location of the studied section (red stars) in the geological map (modified from Choukroune and Séguret, 1973) where the regional cleavage planes are marked with short blue lines. **(B)** The PETM general stratigraphy modified from Barnolas and Gil-Peña (2001), Robador et al. (2010), and Pujalte et al. (2016). Epoch, Age, Geomagnetic Polarity Time Scale (GPTS), C: chrons, and SBZ: Shallow Benthic Zones (SBZ) (Serra-Kiel et al., 1998). Brown colors represent limestones; blue and white colors represent turbiditic deposits. Formation names and litostratigraphic units are represented.

gulf opening to the Bay of Biscay (Plaziat, 1981; Baceta et al., 2011). Reconstructions of the South Pyrenean Basin during the early Paleogene can be found in Baceta et al. (2004), Robador (2008), Pujalte et al. (2016) studies. The deposition of the Paleogene in this South Pyrenean Basin is conditioned by the coeval formation of tectonic structures in the area with the activity of La Foradada fault (Ilerdian-Cuisian = Ypresian, possibly beginning in the Paleocene) and in the eastern part of the studied area with the activity of the Montsec thrust (Paleocene-Cuisian) (Fernández et al., 2012). To the north of the studied area, the activity of the Gavarnie and Millares thrusts has been described during Paleocene-Eocene times (Martinez-Peña and Casas-Sainz, 2003) and to the northeast, the Cotiella and Nogueres thrusts (Vergés et al., 2002; Beamud et al., 2011). Toward the northwest, the Lakora-Eaux-Chaudes was also active (Teixell, 1996; Labaume et al., 2016).

However, the relative tectonic quiescence during the early Paleogene in the studied area contrasts with the highly tectonically active Eocene epoch in the west central part of the Pyrenees (Teixell, 1996; Barnolas and Gil-Peña, 2001; Fernández et al., 2012; Muñoz et al., 2013). A general transgressive stepwise sequence starts in the South-Pyrenean Basin in the Paleocene until the end of the Ilerdian with shallow platform deposits (Puigdefàbregas and Souquet, 1986; Barnolas and Gil-Peña, 2001). An intermediate regression step represented by siliciclastic facies in the northern sections at the beginning of the Ilerdian is interpreted as a braid delta system, fed by river(s) draining the Ebro Massif, which is named La Pardina Fm (Robador et al., 2009; Pujalte et al., 2016) (**Figure 1B**). In the southern studied sections, there is no record of La Pardina Fm (Robador et al., 2009; Pujalte et al., 2016) indicating that the coast retreated northwards, leaving the southern areas emerged for few hundreds of kyr <140–220 kyr according to Pujalte et al. (2016). Subsequently, the study area became submerged by the accumulation of shallow platform sediments (Van de Velde, 1967; Van Lunsen, 1970; Barnolas and Gil-Peña, 2001).

The inversion of the South Pyrenean Basin occurs with the formation of the Pyrenees. The Pyrenees is a WNW-ESE asymmetric mountain range with a mainly southward vergence constituted by thrust sheets involving basement rocks and Mesozoic-Cenozoic cover units (Séguret, 1972; Muñoz, 1992). The formation of the Pyrenees has existed since Late Cretaceous to Miocene times (Roest and Srivastava, 1991). The Range shows a maximum shortening of 147 km at its central eastern part, ∼75% of which is related to the stacking of the basement thrust sheets (Muñoz, 1992). Cleavage developed during the Pyrenean deformation with an estimated related shortening between 15 and 30% (Holl and Anastasio, 1995). This deformation has to be taken into account for a proper reconstruction of the studied

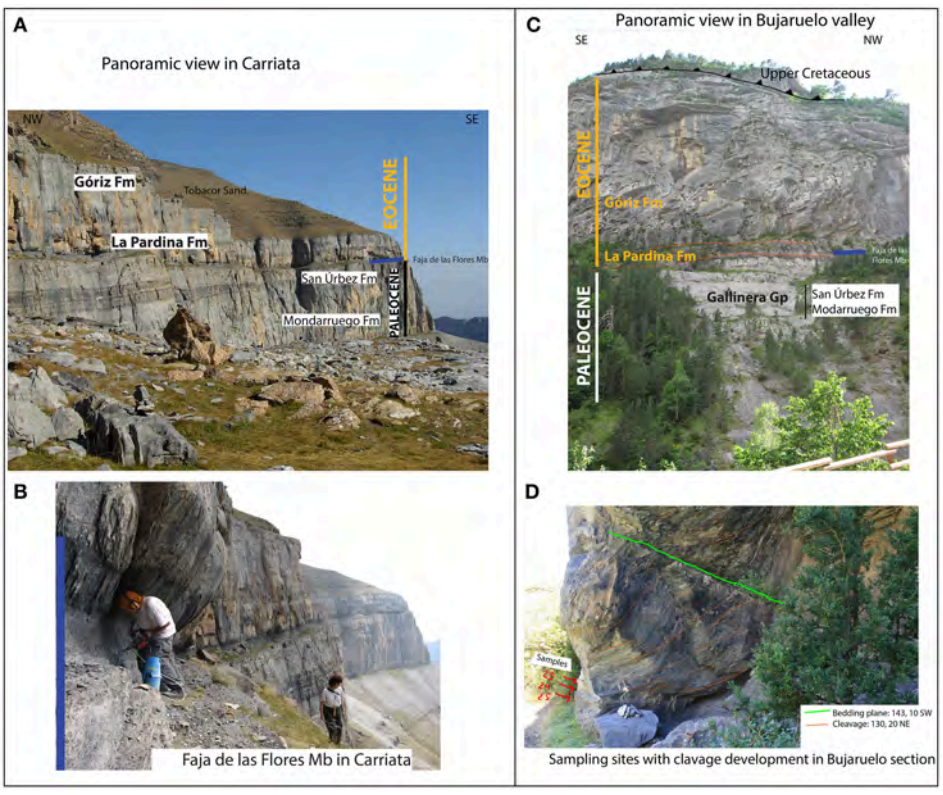

FIGURE 2 | Pictures showing the Gallinera Gp, the PETM of La Pardina Fm, and the Faja de las Flores Mb, **(A)** Panoramic view of Carriata section, **(B)** detail of Faja de las Flores Mb, **(C)** panoramic view of Bujaruelo section, and **(D)** details of sampling site with cleavage and bedding planes.

sections location during the PETM. The deformation of the sections decreases from north to south.

The Carriata and Bujaruelo sections are located in the Internal Sierras, a WNW-ESE high relief area involving Upper Cretaceous and Paleogene marine rocks (**Figure 2**). The Internal Sierras are affected by the south-vergent Larra-Monte Perdido thrust and fold system developed from middle Lutetian to Bartonian times, an imbricated thrust system affecting cover rocks (e.g. Teixell, 1996) (**Figure 3**). Although Carriata and Bujaruelo sections are separated by <5 km today, as it can be seen in **Figures 3a,b**, they are located in the hanging wall and footwall of a thrust related to the Larra-Monte Perdido thrust and fold system, respectively. The displacement of this thrust has been estimated to around ∼10 km (Teixell, 1996; Oliva-Urcia, 2004) (**Figure 3**).

The Gallisué and Entremón sections are located in the Ainsa oblique zone (Muñoz et al., 2013), at present 14 and 39 km to the south, respectively, from the Carriata and Bujaruelo profiles (**Figure 1**). The Ainsa oblique zone represents a thrust and fold system characterized at surface by several north-south kilometer-scale folds. The Gallisué and Entremón sections are located on the western limbs of two of these folds, the Añisclo and Mediano anticlines, respectively (**Figures 1**, **3**, **4**). During the Middle-Late Eocene, structures of the Ainsa oblique zone developed and underwent clockwise vertical axis rotation of more than 50° (Mochales et al., 2012; Muñoz et al., 2013 and references therein). The rotation recorded in the western limb of the Mediano anticline is ∼30° (Bentham, 1992) and similar values are found in the Añisclo anticline (compilation in Muñoz et al., 2013). The pivot point for these clockwise rotations is located at the northwestern end of each lateral ramp they are related to (as suggested in Muñoz et al., 2013). However, in W-E cross-sections (**Figure 3c**, simplified from Fernández et al., 2012), it can be observed that the shortening due to the anticline development is small, the Gallisué section

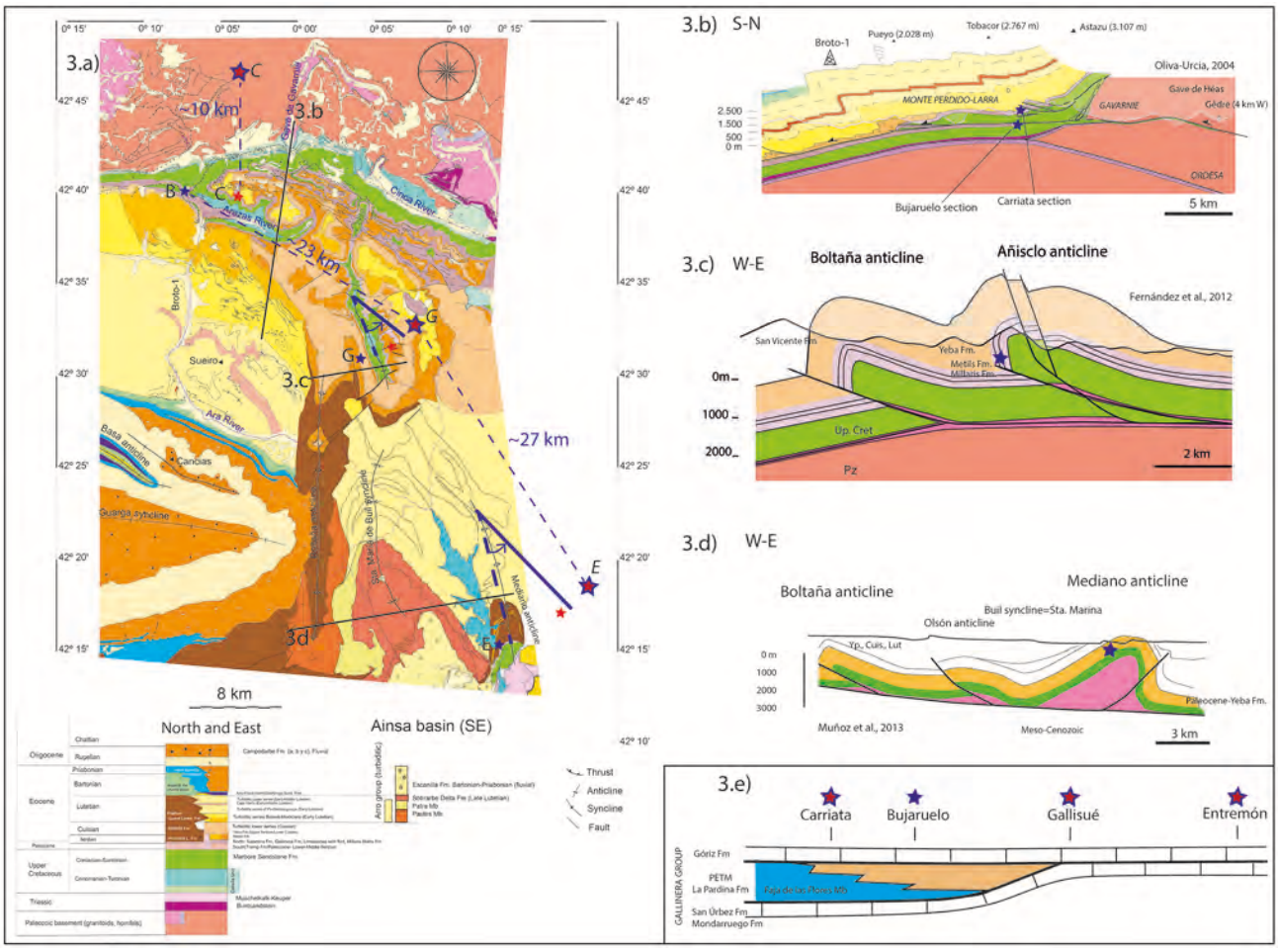

FIGURE 3 | Location of samples with more detail in **(a)** map view and cross-sections **(b)**, **(c)** and **(d)**. Shortening related to thrust and fold systems is ∼10 km in the North, but <2 km for the E-W structures. Red stars locate the sections after restoration of the rotation (in case of the anticlines an anticlockwise rotation of 30° has been performed). Red stars with blue rim are locations of sections after individual rotation restoration and ∼3 km of shortening restoration due to folding. The Bujaruelo section is the one with relative fixed position. C: Carriata, B: Bujaruelo, G: Gallisué, E: Entremón (in italics, the individually restored position of the sections). **(e)** Relative locations at the PETM time, adapted after Pujalte et al. (2016) and Robador et al. (2009) (in blue: prodelta sediments, in yellow: deltaic front).

FIGURE 4 | (a) Panoramic view of the Eocene western limb of the Añisclo anticline, **(b)** the transition of the Paleocene to the Eocene (Thanetian-Ilerdian) masked by karstification, **(c)** a sampled site with two pressure solution family planes (E_0: pressure solution planes parallel to bedding planes; E_1: pressure solution planes related to the alpine deformation, tilt to the east in this outcrop), and **(d)** Photograph of the western limb of the Mediano anticline showing the sampled rocks of the Entremón section. The dam of the Mediano reservoir appears on the left.

was <3 km to the east (not taking into account the clockwise rotation) before the detachment and associated folding took place. Similarly, the shortening due to the Mediano fold is <3 km (**Figure 3d**), simplified from Muñoz et al. (2013). The clockwise rotations imply that originally the Gallisué and Entremón sections were located further to the NE (**Figure 3a**), purple stars with blue rim, after simple restoration of individual structures.

All sections were deposited in a more or less relatively tectonic quiescence and were later incorporated into the Pyrenean proto-chain during Lutetian to Bartonian times (e.g., Teixell, 1992, 1996; Poblet et al., 1998; Muñoz et al., 2013).

The cleavage developed during the alpine deformation revealed the internal deformation, the paleotemperatures, and the tectonic load under which the pressure solution cleavage during the Pyrean orogeny occurred. The dominant cleavage is axial planar to folds at different scales in the studied area. The cleavage development is mainly related to the Gavarnie thrust emplacement and affects Paleozoic, Triassic, Upper Cretaceous, Paleocene, and the lower part of the turbiditic sequence of the Eocene Hecho Group in the studied area (Choukroune et al., 1968; Labaume et al., 1985; Teixell, 1992; Holl and Anastasio, 1995; Rodríguez Méndez, 2011; Izquierdo-Llavall et al., 2013). The analyses of 56 samples were carried out using petrographic and microthermometric analyses of fluid inclusions in extensional veins. The X-ray diffraction on clay mineral assemblages and the optical analysis (with vitrinite reflectance analysis) on organic matter dispersed in the sedimentary succession allowed to deduce paleotemperatures of 140–160° up to 215°C, which required a minimum burial for cleavage development of ∼4km in the Internal Sierras (Izquierdo-Llavall et al., 2013).

The development of cleavage was at first identified as a possible mechanism for a regional remagnetization found in the Internal Sierras, which postdates folding and tilting linked to the Gavarnie emplacement (Oliva-Urcia and Pueyo, 2007; Oliva-Urcia et al., 2008). In addition, detailed investigations in the area revealed that the presence of a previous diachronic remagnetization event that predates the tilting of the Gavarnie thrust (Izquierdo-Llavall et al., 2015). The Carriata, Bujaruelo, and Gallisué sections analyzed in this study are located within the regional cleavage development area, which also corresponds

to the remagnetized rock area (**Figures 1**, **2D**). The regional knowledge of the PETM in the sampled sections has prompted their magnetic characterization in order to detect a diagnostic and preserved magnetic signal of that event despite subsequent diagenetic and deformational processes. Thus, four sections have been studied.

METHODS

The Paleocene-Eocene in the Southwest central Pyrenees is characterized by the following carbonatic rocks: marls, dolostones, limestones, sandy limestones, and marly limestones. Stratigraphic field observations are complemented with bibliographic definitions of SBZ and recent updates of names of Formations (Fm). As explained by Pujalte et al. (2016), the Gallinera Fm of Van de Velde (1967) is now considered the Gallinera Group, comprising the Fms of Mondarruego (limestones), San Úrbez (sandy limestones), Pardina (siliciclastic), and Góriz (limestones) (Robador et al., 2010).

In the Carriata section, three levels were sampled from the Salarons Fm (dolostones) and the rest of the samples were taken from Mondarruego, San Úrbez, La Pardina, and Góriz Fms in ∼130 m of section (**Figure 5**, **Table 1**). In Bujaruelo section, samples were taken from San Úrbez and La Pardina Fms for ∼40 m, 17 m of which are from the siliciclastic part of La Pardina Fm (**Figure 5**, **Table 1**). In the Gallisué section, samples were taken from the Mondarruego (∼90 m), San Úrbez (∼50 m), and La Pardina (∼42 m) Fms. The Faja de las Flores Mb is not present (**Figure 5**, **Table 1**). In the Entremón section (named Mediano section in Pujalte et al., 2016), sampling was performed for ∼70 m in the upper part of the Mondarruego, San Úrbez, and La Pardina Fms (**Figure 5**, **Table 1**).

Classical Rock Magnetic and Paleomagnetic Analyses

Paleomagnetic samples of standard size were drilled with a gasoline-powered portable water-cooled drill machine. Each section has 88, 54, 47, and 152 samples from Carriata, Bujaruelo, Gallisué, and Entremón sections, respectively. Sampling space varies from 0.5 to 8 m.

The rock magnetic measurements comprise the following: bulk magnetic susceptibility (χ), natural remanent magnetization (NRM), anhysteretic remanent magnetization (ARM), saturation of isothermal remanent magnetization (SIRM), and coercivity of remanence (Hcr). The DC field imposed over 100 mT alternating

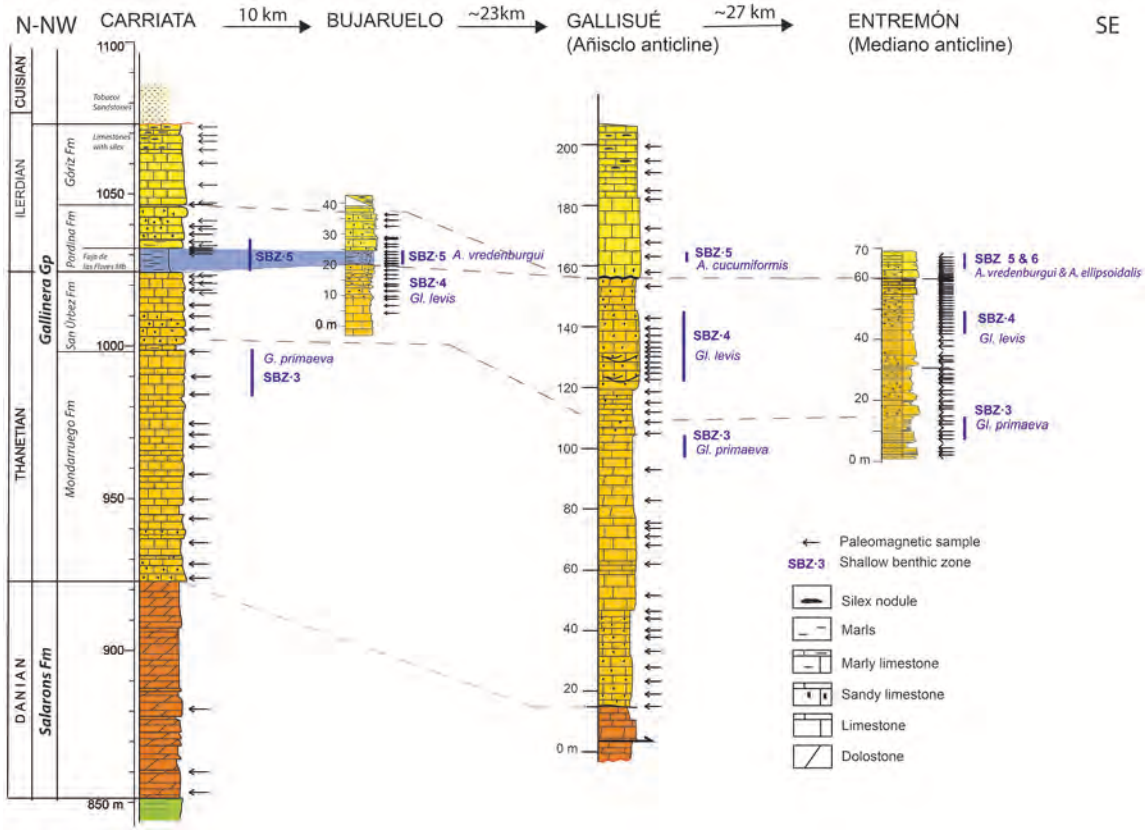

FIGURE 5 | The four sections located from N-NW to SW with distances between each section after simple deformation reconstruction. Age represented on the left. For each column and from left to right, the following are shown: Stratigraphy (Fm names), representation of lithology and age, sampling distances (marked by arrows), and SBZ. The blue thick bar points to the Faja de las Flores Mb (Robador et al., 2010; Pujalte et al., 2016).

TABLE 1 | Averages for the paleomagnetic component calculated in each section.

Section	Identifier	n/N	Unblock T (°)/mag. field (mT)	Geographic				Bedding		Tilt corrected			
				Dec. (°)	Inc. (°)	α_{95}	*k*	Strike (°)	Dip (°)	Dec. (°)	Inc. (°)	α_{95}	*k*
Carriata	MON	19/38	325–425	197	−39	6	50	0	0				
Bujaruelo	BU	24/47	300–400	206	−46	9	12	123	24W	198	−69	10	12
Añisclo valley (out of sections)	AN1	7/14	350–450	201	−35	5	122	22	29E	220	−30	5	192
Gallisué	SEC1	10/37	325–450/40–80	179	−29	18	9	155	28W	160	−37	18	9
	SEC2	0/26	–	–	–	–	–	157	35W				
	SEC3	2/18	325–425	176	−33	38	91	152	33W	152	−40	38	91
	SEC4	7/7	325–425/40–80	166	−38	12	31	151	35W	140	−38	12	31
	EST1	9/10	325–425/40–80	190	−27	6	74	151	41W	161	−45	6	74
	EST2	14/14	375–425/40–70	178	−34	9	24	158	40W	147	−35	7	38
	EST3	21/27	40–80	186	−30	9	14	162	41W	159	−37	9	14
	193–202	9/13	325–450/40–70	198	−39	10	31	4	89W	144	−11	10	31
	203–226	11/16	325–425/40–70	204	−35	14	14	143	36W	175	−62	14	14
Entremón	EN	0/31	–	–	–	–	–	002	46W				

In Gallisué section, sites were grouped along the section. Name of section; identifier; number of samples (n) used from the total (N) for average; unblocking temperature in °C (field in mT); Dec., declination; Inc., inclination; α95 and k, statistical parameters associated with the means; bedding (strike and dip); geographic, before tectonic correction; and tilt corrected, after tectonic correction.

field (AF) demagnetization of the ARM was 50 μT in the ARM Magnetizer (2G Entrerprises). The maximum applied field for the SIRM varies from 0.5 to 1.8 T, applied with a pulse demagnetizer. The Hcr was calculated after the saturation of the sample at 0.5 T or 1.8 T. All measurements were performed at room temperature and normalized by mass. The coercivity of the remanence was calculated after applying the maximum field to the standard samples and then applying a magnetic field with increasing steps on the contrary sense or with powered samples in a magnetic measurements variable field translation balance (MMVFTB) as explained later.

The variations of the bulk susceptibility, ARM, and SIRM are presented. The ARM reflects the concentration of low coercivity minerals (magnetite or ferromagnetic iron sulfides). The SIRM at high fields reflects the concentration of the antiferromagnetic minerals (minerals with high coercivity: hematites, goethite) plus the ferromagnetic minerals (Oldfield, 1991; Hunt et al., 1995; Ortega et al., 2006; Wang et al., 2010). The SIRM/ARM ratio, on the other hand, reveals the magnetic grain size variations in the section when a single magnetic mineralogy is present (Peters and Dekkers, 2003).

For paleomagnetic analyses, most specimens were subjected to stepwise AF demagnetization procedures. Some sister samples also were stepwise thermally (TH) demagnetized. A total of 315 standard size paleomagnetic samples were analyzed. In addition, to perform the fold test at regional scale, discrete standard paleomagnetic samples were taken in the Añisclo anticline to the east and west of the Gallisué section in the Upper Cretaceous and Eocene rocks, respectively. Acquisition curves of isothermal remanent magnetization (IRM) (Dunlop, 1972) were also performed in some representative samples.

The rock magnetic and paleomagnetic measurements have been performed in different laboratories: Paleomagnetic Laboratory of Burgos University and the Paleomagnetic Laboratory of Barcelona (CCiTUB -CSIC) in Spain, Kochi Core Center (Kochi University/JAMSTEC, Japan), and New Mexico University (Albuquerque, USA) using cryogenic magnetometers (2G Enterprises, Mountain View, CA, USA) with AF coils for the alternating field demagnetizations and zero fields ovens for the thermal demagnetization (every 50 to 25°C in ovens: Model TSD-1 Thermal Specimen Demagnetize—Schonstedt Instument Co. and MMTD—Magnetic Measurements Ltd., Aughton, UK) and every 5–20 mT steps in the AF coils. The characteristic components were calculated using the principal component analyses (PCA) (Kirschvink, 1980) with the VPD software (Ramón et al., 2017) and Remasof (Chadima and Hrouda, 2007). Fold tests were performed to determine the relative age of a characteristic component with respect to folding, at profile and regional scale using the IAPD-32 program (T. Torsvik et al., Software IAPD-32, 1996), which follows criteria from McElhinny (1964) and software from McFadden (1990).

Bulk magnetic susceptibility (χ) was measured in a KLY-3S Kappabridge (working at 300 A/m and 875 Hz, AGICO Inc., Czech Republic) at the University of Zaragoza (Spain).

Twenty selected samples were powdered to analyze their magnetic mineralogy. A MMVFTB (Petersen Instruments Mag-Instruments UG—Munich, Germany—) was used to measure the thermomagnetic curves (measuring variations of the induced magnetization between room temperature and 700°C in an applied field of 38 mT).

RESULTS

Stratigraphy

The carbonatic rocks studied in the Carriata section start with the Paleocene rocks overlying the Maastrichtian (Upper Cretaceous),

which consists of ∼70 m of dolostones, limestones, and dolomitic limestones with algae laminations and scarce fossil content, which are known as Salarons dolostones Fm (Van de Velde, 1967). Its lower boundary is an abrupt lithological change with the siliciclastic deposits of the Maastrichtian Marboré Sandstones Fm. On top of the Salarons Fm, the Gallinera Gp is about 150 m. As explained by Pujalte et al. (2016), the Gallinera Fm of Van de Velde (1967) is now considered the Gallinera

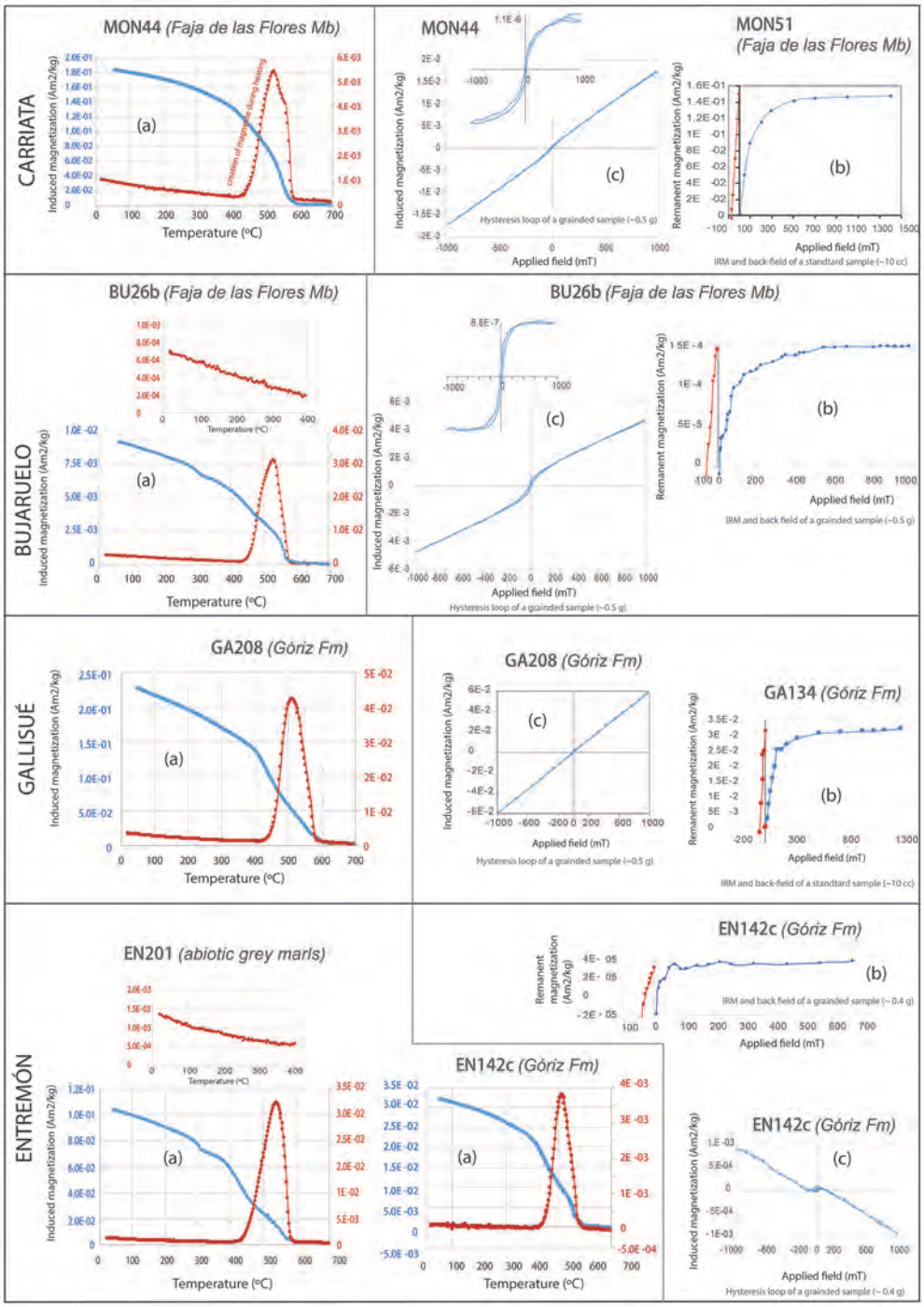

FIGURE 6 | (a) Curves of induced magnetization as a function of temperature (notice the different scale for the heating with respect to the cooling curves). The main decay of the heating run (red) at 580°C corresponds to the Curie temperature of magnetite. **(b)** Acquisition of the isothermal remanent magnetization (blue) and back-field (red) curves and **(c)** hysteresis loops (analyzed in a MMVFTB). MON: Carriata section, BU: Bujaruelo section, GA: Gallisué section, and EN: Entremón section.

Group, comprising the Fms of Mondarruego (limestones), San Úrbez (sandy limestones), Pardina (siliciclastic), and Góriz (limestones) (Robador et al., 2010) shown in **Figure 5**. The Mondarruego Fm in the Carriata section is ∼75 m thick; it begins with 10 m of sandy limestones with discocyclines, nummulites, operculiniforms, and local corals. The upper part of the Mondarruego Fm in this section contains benthic foraminifera: *Glomalveolina primaeva*, characteristic of SBZ3 (Serra-Kiel et al., 1998), of Lower-Middle Thanetian age. Overlying the Mondarruego Fm, there is San Úrbez Fm, which starts with ∼10 m of sandy limestones and sandstones with tractive structures. In the upper part of the San Úrbez Fm,

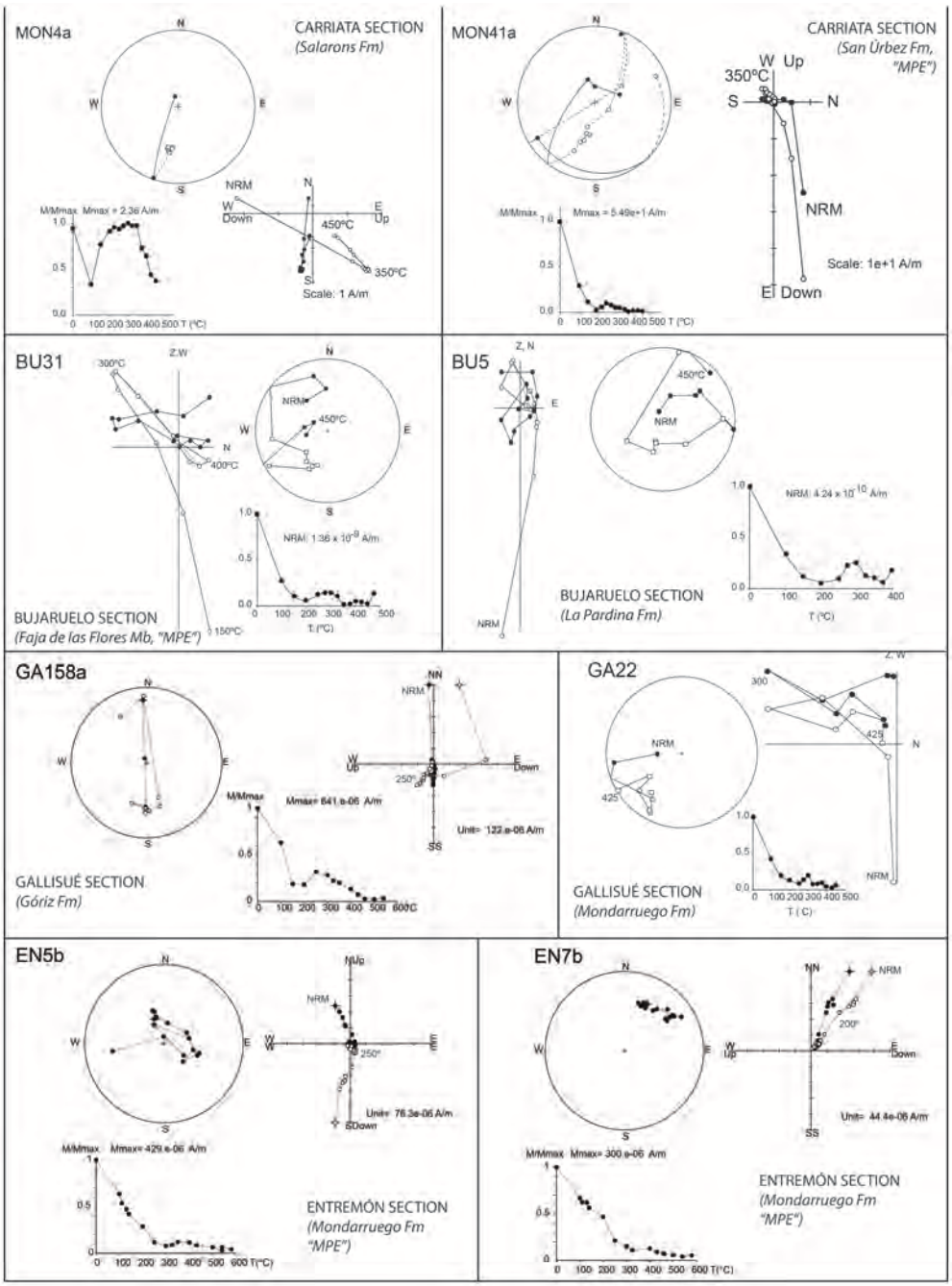

FIGURE 7 | Examples of thermal demagnetization diagrams in stereographic and orthogonal projections and NRM decay during the stepwise demagnetization procedure. Open (closed) symbols represent down (up) directions, respectively. "MPE": magnetic properties excursion, marked by blue (gray) bars in **Figure 8** (**Figure 9**).

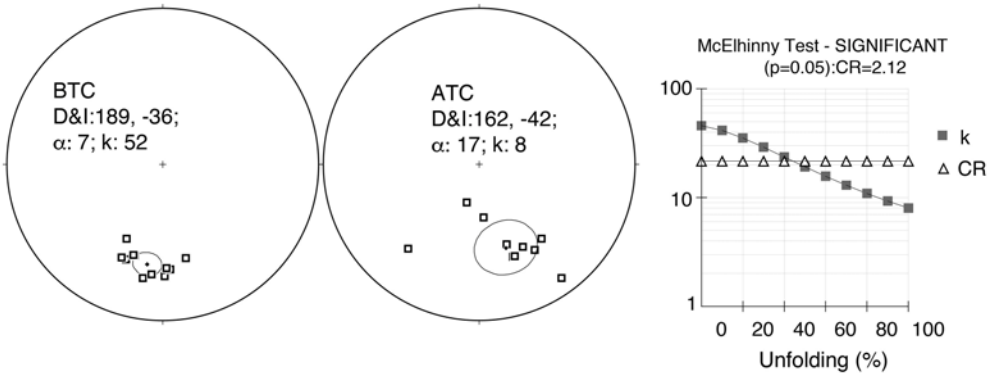

FIGURE 8 | McElhinny's fold test for the characteristic component in the sampled rocks. Equal-area projections are before (BTC) and after (ATC) tectonic correction. The fold test is significant and negative. The CR (CR: critical value) depends on the number of samples and their vectorial sum. The test is positive when k>CR and maximum at 100% unfolding, and it is negative when k>CR and maximum at 0% unfolding of the bedding planes.

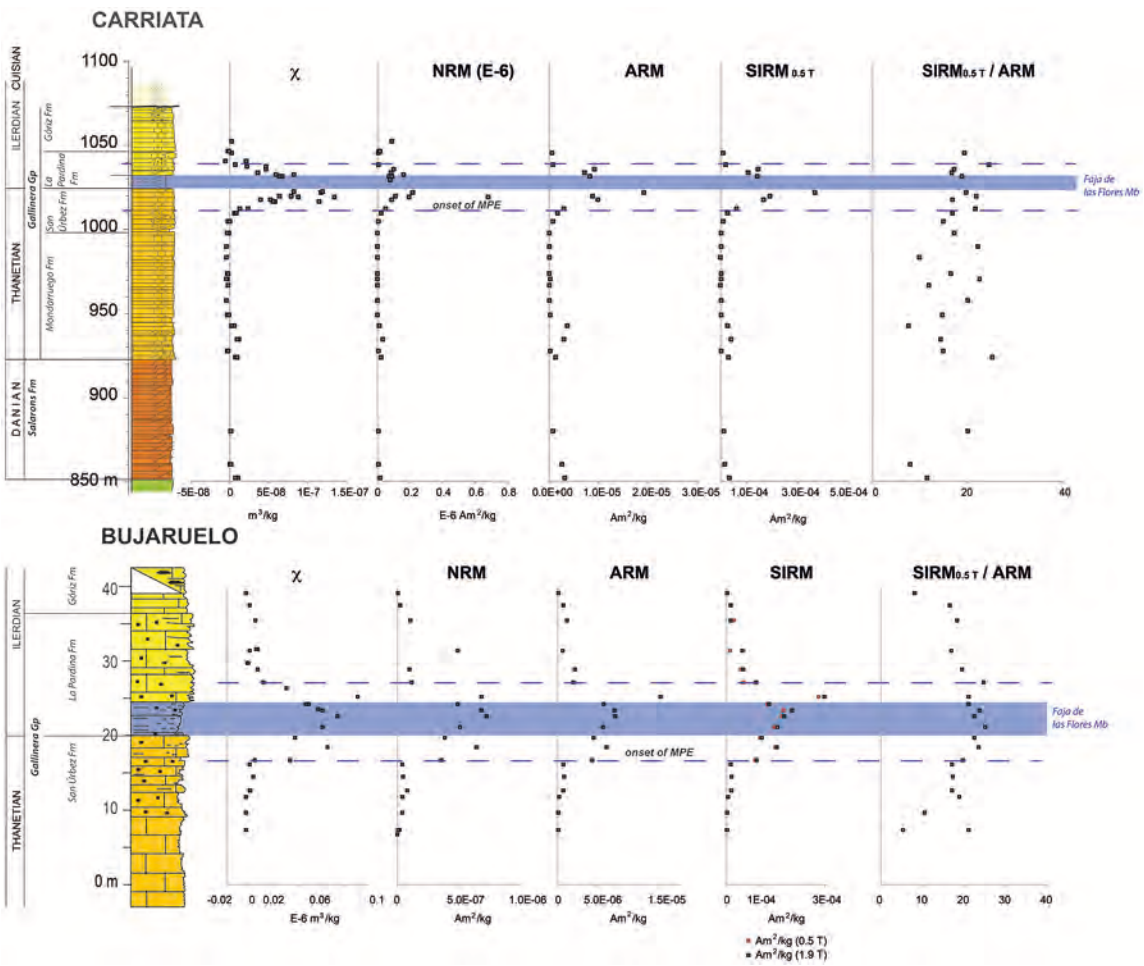

FIGURE 9 | Magnetic signal in Carriata and Bujaruelo sections, bulk magnetic susceptibility, NRM, ARM, SIRM, and $SIRM_{0.5T}$/ARM ratio. Discontinuous horizontal blue lines mark the positive "magnetic properties excursion" (MPE). The blue rectangle marks the Faja de las Flores Mb at the bottom of La Pardina Fm (following Pujalte et al., 2016). Vertical scale is variable. In the Bujaruelo section, the colors of the SIRM column represent two different applied fields: in red, 0.5 T and in gray, 1.9 T.

there are limestones rich in macroforaminifera (*Ranikothalia*) assigned to SBZ4 and attributed to the Upper Thanetian. In sharp contact overlying Thanetian limestones, 10 m of black marls crop out (the Faja de las Flores Member –Mb–), with a limolite-sandy level on top. They contain large foraminifera and have been related to the PETM (Pujalte et al., 2016). Overlying them, 18 m of sandy and marly limestones evolve to limestones rich in alveolinids, both the Faja de las Flores Mb together with the 18 m of sandy limestones fm La Pardina Fm. The faunal content of this unit has been assigned to the lower Ilerdian SBZ5 and SBZ6 (*A. cucumiformis* biozone). The section ends with 10 m of well-bedded limestones that are rich in chert nodules of the Góriz Fm. Regionally, brown marls and marly limestones of the Millaris Fm, attributed to the Middle Ilerdian, overlie the Góriz Fm with a sharp contact, but in this section, the Millaris Fm has been eroded by the Tobacor Sandstone Fm (Hecho Group turbidites, Bolave Mondiciero type, Ríos et al., 1982).

In Bujaruelo section, limestones and sandly limestones were sampled (San Úrbez and La Pardina Fms). In the lower part of the San Úrbez Fm, macroforaminifera related to SBZ4 were distinguished in the field (*Glomalveolina levis).* In this section, the Faja de las Flores Mb is ∼5 m thick and shows a pervasive cleavage development as in the Carriata section (**Figures 2B,D**), *Alveolina bredenburgui* was identified in the Faja de las Flores Mb (SBZ5, Serra-Kiel et al., 1998).

In the Gallisué section, samples were taken from the Mondarruego (∼90 m), San Úrbez (∼50 m) and La Pardina (∼42 m) Fms. The Faja de las Flores Mb is not present. *Glomalveolina primaeva* (SBZ3, Serra-Kiel et al., 1998) was identified at the top of the Mondarruego Fm. *Glovalveolina levis* is present in the San Úrbez Fm. The lower part of the

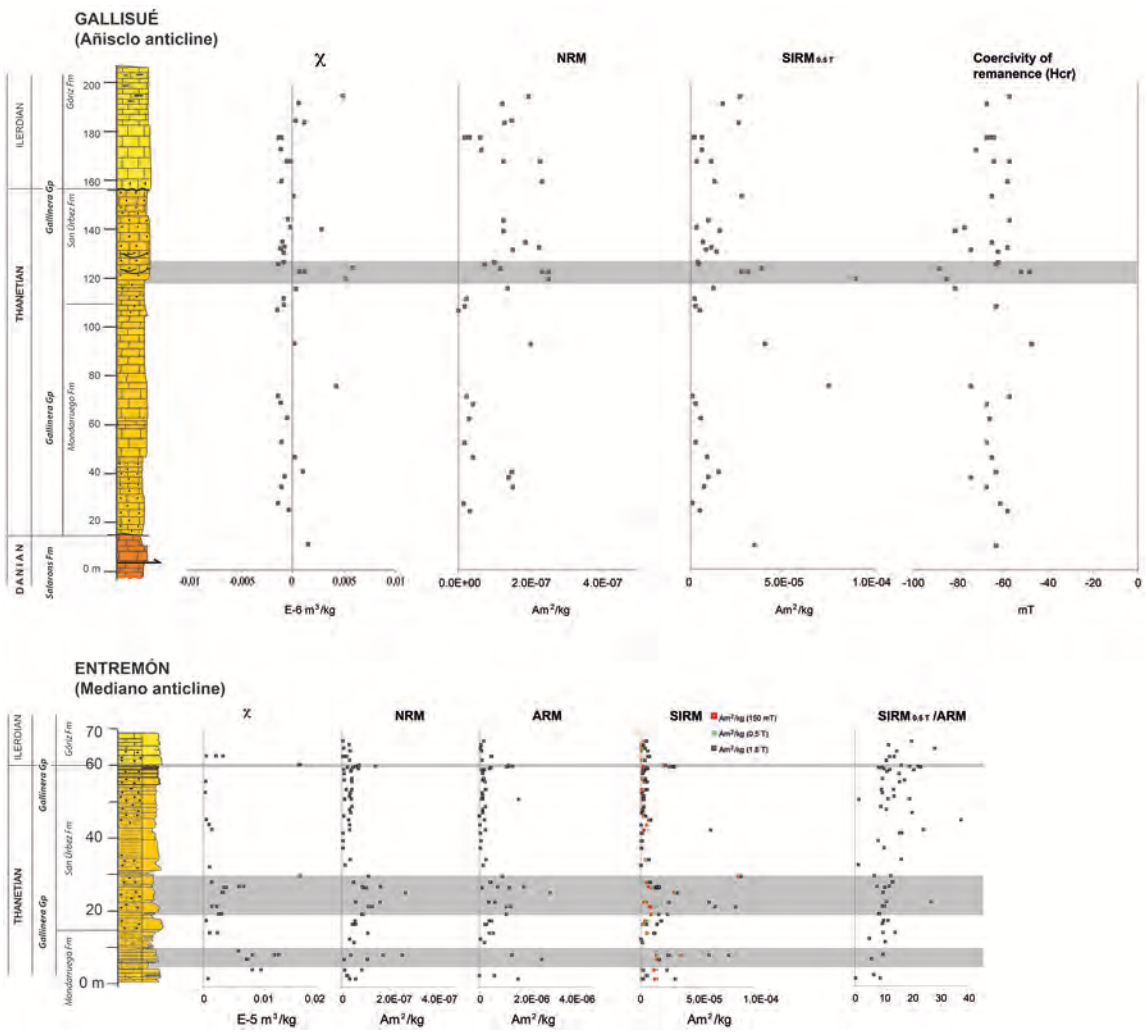

FIGURE 10 | Magnetic signal in the Gallisué and the Entremón sections. In Gallisué, bulk magnetic susceptibility, NRM, $SIRM_{0.5T}$, and coercivity of the remanence (mT). In Entremón, bulk magnetic susceptibility, NRM, ARM, SIRM, and $SIRM_{0.5T}$/ARM ratio. The colors of the SIRM column represent three different applied fields: in red, 150 mT, in green, 0.5 T, and in gray, 1.8 T. Gray bar marks higher values of ARM and/or SIRM. In the Entremón section, the top gray bar corresponds to the abiotic marly interval. Vertical scale is variable.

TABLE 2 | Magnetic properties normalized by mass of the samples in the four sections.

(A) CARRIATA

χ Site	Position (m)	χ (m^3/kg)	NRM Site	Position (m)	NRM (Am^2/kg) E 10-6	ARM Site	Position (m)	ARM (Am^2/kg)	SIRM (0.5 T)	Position (m)	SIRM (0.5 T) (Am^2/kg)
MON1a	852	1.04E-08	MON2B	852	1.65E-02	MON1a	852	3.04E-06	MON1a	852	3.23E-05
MON2a	852	7.35E-09	MON-4A	860	7.77E-03	MON3a	860	2.51E-06	MON3a	860	1.71E-05
MON3a	860	3.71E-10	MON-6A	880	8.57E-03	MON5a	880	6.76E-07	MON5a	880	1.26E-05
MON4b	860	1.05E-09	MON-8A	924	2.39E-02	MON7a	924	1.29E-06	MON7a	924	3.13E-05
MON5a	880	1.66E-09	MON-10A	928	5.47E-03	MON9a	928	2.46E-07	MON9a	928	3.31E-06
MON7a	924	7.22E-09	MON-12A	935	3.42E-02	MON11a	935	2.97E-06	MON11a	935	3.93E-05
MON8a	924	9.19E-09	MON-13A	943	1.20E-02	MON13b	943	3.59E-06	MON13b	943	2.69E-05
MON9a	928	−2.93E-09	MON-15A	949.5	8.16E-04	MON16a	949.5	1.50E-07	MON16a	949.5	2.16E-06
MON10b	928	−1.65E-09	MON-18A	958	3.74E-04	MON17a	958	5.58E-08	MON17a	958	1.05E-06
MON11a	935	1.17E-08	MON-20A	967	4.48E-04	MON19a	967	4.55E-08	MON19a	967	5.02E-07
MON12b	935	8.99E-09	MON-21A	971	1.10E-03	MON21a	971	1.20E-07	MON21a	971	2.72E-06
MON13b	943	5.94E-09	MON-24A	974	9.60E-04	MON23a	974	9.82E-08	MON23a	974	1.56E-06
MON14a	943	2.66E-09	MON-25A	984	3.79E-04	MON26b	984	5.78E-08	MON26b	984	5.52E-07
MON15b	949.5	−3.84E-09	MON-27A	990	1.98E-04	MON28b	990	5.28E-08	MON28b	990	1.23E-06
MON16a	949.5	−1.31E-09	MON-30A	998	1.06E-03	MON29b	998	7.94E-08	MON29b	998	1.30E-06
MON17a	958	−4.16E-09	MON-31A	1005	5.40E-03	MON32A	1005	6.74E-07	MON32A	1005	9.96E-06
MON18b	958	−4.24E-09	MON-34A	1010	2.04E-02	MON33A	1010	1.59E-06	MON33A	1010	2.68E-05
MON19a	967	−1.98E-09	MON-35A	1013	4.92E-02	MON35B	1013	2.99E-06	MON35B	1013	6.22E-05
MON21a	971	−3.78E-09	MON-38A	1018	8.91E-02	MON37B	1018	9.77E-06	MON37B	1018	1.66E-04
MON22a	971	−3.94E-09	MON-40A	1020.5	1.10E-01	MON40B	1020.5	8.76E-06	MON40B	1020.5	1.92E-04
MON23a	974	−2.78E-09	MON-41A	1022.5	2.16E-01	MON42A	1022.5	1.91E-05	MON42A	1022.5	3.66E-04
MON24b	974	−2.69E-09	MON-44A	1030	7.92E-02	MON51A	1032	8.22E-06	MON51A	1032	1.42E-04
MON26b	984	−3.98E-09	MON-52A	1032	7.25E-02	MON54A	1034	7.19E-06	MON54A	1034	1.08E-04
MON28b	990	−4.16E-09	MON-53A	1032	8.65E-02	MON56B	1036.5	9.06E-06	MON56B	1036.5	1.44E-04
MON29b	998	−8.71E-10	MON-55	1034	8.32E-02	MON58A	1039	8.25E-07	MON58A	1039	1.85E-05
MON30b	998	−3.49E-09	MON-56A	1036.5	9.84E-02	MON60A	1046	6.17E-07	MON60A	1046	1.12E-05
MON31B	1005	−2.20E-09	MON-59A	1039	7.58E-03						
MON32A	1005	−1.25E-10	MON-61A	1046	7.92E-03						
MON33A	1010	5.38E-09	MON-83A	1020	1.97E-01						
MON34B	1010	7.85E-09	MON-84A	1020	6.82E-01						
MON35B	1013	2.31E-08	MON-87A	1033	1.62E-01						
MON36B	1013	1.32E-08	MON-88B	1033	1.66E+00						
MON37B	1018	3.90E-08	MON-90A	1038	1.80E+00						
MON38B	1018	5.16E-08	MON-93A	1047	1.10E-02						
MON39A	1020.5	6.36E-08	MON-94A	1047	1.55E-02						
MON40B	1020.5	7.84E-08	MON-96A	1053	8.77E-02						
MON54A	1034	3.61E-08									
MON56B	1036.5	4.62E-08									
MON58A	1039	7.21E-09									
MON60A	1046	2.23E-09									
MON80A	1017	5.79E-08									
MON81A	1017	5.55E-08									
MON82B	1017	1.14E-07									
MON83B	1020	8.85E-08									
MON84B	1020	1.34E-07									
MON85B	1023	1.19E-07									
MON86A	1023	8.19E-08									

(Continued)

TABLE 2 | Continued

(A) CARRIATA

χ Site	Position (m)	χ (m^3/kg)	NRM Site	Position (m)	NRM (Am^2/kg) E 10-6	ARM Site	Position (m)	ARM (Am^2/kg)	SIRM (0.5 T)	Position (m)	SIRM (0.5 T) (Am^2/kg)
MON87B	1033	8.18E-08									
MON88A	1033	5.87E-08									
MON89A	1038	4.62E-08									
MON90B	1038	2.23E-08									
MON91A	1041	2.04E-08									
MON92A	1041	−5.12E-09									
MON93B	1047	−2.48E-09									
MON94B	1047	−6.62E-10									
MON95A	1053	2.05E-09									

(B) BUJARUELO

χ Site	Position (m)	χ (m^3/kg)	NRM Site	Position (m)	NRM (Am^2/kg)	Site	Position (m)	ARM (Am^2/kg)	SIRM (0.5 T & 1.9 T)	Position (m)	SIRM (0.5 T) (Am^2/kg)	SIRM (1.9 T) (Am^2/kg)
53b	7.3	−3.88E-03	54a	6.8	7.98E-10	53b	7.3	5.87E-08	53b	7.3	1.24E-06	1.60E-06
52a	7.3	−4.30E-03	53b	7.3	1.53E-08	52a	7.3	5.34E-08	52a	7.3	2.86E-07	7.71E-07
50a	9.7	−4.14E-03	52a	7.3	3.93E-09	50a	9.7	8.45E-08	50a	9.7	8.84E-07	1.80E-06
49b	11.8	−4.32E-03	50a	9.7	4.14E-08	48a	11.8	1.44E-07	48a	11.8	2.72E-06	3.63E-06
48a	11.8	−4.01E-03	48a	11.8	3.90E-08	46b	12.7	7.50E-07	46b	12.7	1.29E-05	1.49E-05
47b	12.7	−9.31E-04	46b	12.7	7.82E-08	44a	14.5	8.33E-07	44a	14.5	1.44E-05	1.52E-05
46b	12.7	−6.26E-04	44a	14.5	4.35E-08	42a	16.1	6.88E-07	42a	16.1	1.17E-05	1.19E-05
44a	14.5	1.71E-03	42a	16.1	4.13E-08	40a	16.7	4.42E-06	40a	16.7	8.73E-05	9.04E-05
43b	16.1	−1.13E-03	40a	16.7	3.52E-07	38a	18.5	6.33E-06	38a	18.5	1.49E-04	1.52E-04
42a	16.1	−9.34E-04	38a	18.5	6.36E-07	36b	19.7	4.61E-06	36b	19.7	1.03E-04	1.06E-04
41b	16.7	3.16E-03	36b	19.7	3.83E-07	34a	21.2	5.81E-06	34a	21.2	1.46E-04	1.54E-04
40a	16.7	3.32E-02	34a	21.2	5.07E-07	32a	22.6	7.46E-06	32a	22.6	1.68E-04	1.74E-04
38a	18.5	6.47E-02	32a	22.6	7.17E-07	28a	23.4	7.33E-06	28a	23.4	1.73E-04	1.99E-04
36b	19.7	3.71E-02	28a	23.4	6.81E-07	24a	24.3	5.90E-06	24a	24.3	1.24E-04	1.29E-04
34a	21.2	6.06E-02	24a	24.3	4.87E-07	22a	25.2	1.33E-05	22a	25.2	2.79E-04	2.97E-04
32a	22.6	7.29E-02	22a	25.2	6.77E-07	18a	27.2	1.99E-06	18a	27.2	4.95E-05	8.91E-05
28a	23.4	6.03E-02	18a	27.2	1.14E-07	14a	28.9	2.21E-06	14a	28.9	4.30E-05	4.96E-05
26a	23.6	5.67E-02	14a	28.9	9.71E-08	10a	31.4	5.84E-07	10a	31.4	9.90E-06	4.75E-05
24a	24.3	4.89E-02	10a	31.4	4.88E-07	6a	35.5	1.17E-06	6a	35.5	2.13E-05	1.24E-05
23b	24.3	4.65E-02	6a	35.5	1.01E-07	4a	37.5	7.52E-07	4a	37.5	1.24E-05	1.34E-05
22a	25.2	9.00E-02	4a	37.5	2.20E-08	2a	39.2	5.64E-08	2a	39.2	4.56E-07	1.37E-06
20a	26.4	3.00E-02	2a	39.2	1.28E-09							
18a	27.2	1.07E-02										
14a	28.9	5.63E-03										
12a	29.8	−2.80E-03										
11b	29.8	−2.49E-03										
10a	31.4	−1.37E-03										
8a	31.6	5.60E-03										
7a	31.6	4.19E-03										
6a	35.5	4.03E-03										
4a	37.5	−1.25E-03										
2a	39.2	−4.17E-03										

(Continued)

TABLE 2 | Continued

(C) GALLISUÉ					
Site	**Position**	**χ**	**NRM**	**SIRM (0.5 T)**	**Coercivity of remanence**
	(m)	**(m^3/kg)**	**(Am^2/kg)**	**(Am^2/kg)**	**(mT)**
GA4b	10	1.66E-03	5.68E-07	3.42E-05	−63
GA5b	24	−2.34E-04	3.18E-08	5.09E-06	−58
GA8b	27	−1.30E-03	1.44E-08	9.45E-07	−61
GA10b	34	−9.10E-04	1.51E-07	7.50E-06	−67
GA11b	38	−6.82E-04	1.41E-07	9.76E-06	−74
GA14b	40	1.19E-03	1.47E-07	1.54E-05	−63
GA17b	46	2.64E-04	4.06E-08	8.88E-06	−65
GA20b	52	−9.57E-04	1.59E-08	2.79E-06	−67
GA22b	62	−3.64E-04	2.86E-08	5.43E-06	−66
GA24b	68	−9.86E-04	3.99E-08	2.60E-06	−67
GA26b	71	−1.23E-03	2.26E-08	1.26E-06	−57
GA30a	75	4.35E-03	8.36E-07	7.47E-05	−74
GA33b	92.5	2.98E-04	2.02E-07	4.02E-05	−47
GA37b	108	−7.83E-04	1.69E-08	2.62E-06	−63
GA39b	111	−7.50E-04	2.15E-08	2.30E-06	−570
GA42b	115	4.43E-04	1.38E-07	1.22E-05	−81
GA43b	119	5.31E-03	2.50E-07	8.96E-05	−85
GA45a	122	1.30E-03	2.33E-07	3.10E-05	−52
GA46b	122	8.58E-04	2.52E-07	2.76E-05	−48
GA47a	123.5	6.01E-03	1.17E-07	3.87E-05	−88
GA49b	125	−1.17E-03	7.36E-08	4.39E-06	−63
GA51b	126	−8.62E-04	9.86E-08	3.70E-06	−62
GA54b	130	−8.55E-04	1.22E-06	1.38E-05	−62
GA55b	131	−9.03E-04	1.52E-07	8.64E-06	−74
GA57b	132	−7.17E-04	2.25E-07	1.14E-05	−58
GA59b	134	−8.22E-04	1.87E-07	6.76E-06	−65
GA63b	139	2.95E-03	1.25E-07	1.59E-05	−81
GA64a	140	−9.54E-05	5.29E-07	2.97E-06	−77
GA66b	143	−3.09E-04	1.25E-07	9.53E-06	−57
GA68a	153	1.75E-04	9.64E-07	2.76E-05	−65
Ga70b	159	−9.01E-04	2.34E-07	1.31E-05	−58
GA73b	167	−1.09E-04	2.27E-07	3.29E-06	−64
GA75a	167	−3.19E-04	1.26E-07	1.13E-05	−57
Ga77b	172	−1.01E-03	6.38E-08	6.14E-06	−72
GA78b	177	−1.21E-03	6.01E-08	1.45E-06	−64
GA80b	177	−1.19E-03	2.49E-08	2.16E-06	−66
GA82b	177	−9.96E-04	1.77E-08	1.47E-06	−67
GA84b	177	−1.13E-03	3.16E-08	6.18E-06	−475
GA88b	183	1.22E-03	1.29E-07	2.60E-05	−105
GA90b	184	4.25E-04	1.47E-07	1.17E-04	−292
GA91a	191	6.82E-04	1.22E-07	1.75E-05	−67
GA97b	200	5.06E-03	1.96E-07	2.64E-05	−57

(Continued)

TABLE 2 | Continued

(D) ENTREMÓN									
Site	**Position (m)**	**χ (m^3/kg)**	**Site**	**Position (m)**	**NRM (Am^2/kg)**	**ARM (Am2/kg)**	**SIRM (150 mT) (Am^2/kg)**	**SIRM (0.5 T) (Am^2/kg)**	**SIRM (1.8 T) (Am^2/kg)**
EN1a	0	−5.03E-04	EN1a	0	3.40E-08	1.15E-05	1.15E-06	1.30E-06	2.22E-06
EN2a	0	7.31E-04	EN2a	0	5.97E-08	1.70E-06	1.28E-05	1.54E-05	3.09E-05
EN3a	0.8	−3.71E-03	EN3a	0.8	2.06E-08	6.56E-07	4.13E-06	4.34E-06	5.66E-06
EN4a	0.8	−4.14E-03	EN4a	0.8	2.36E-08	-	4.17E-06	4.38E-06	6.01E-06
EN5a	2.3	8.62E-03	EN5a	2.3	8.79E-08	-	1.15E-05	1.45E-05	2.35E-05
EN6a	2.3	1.01E-02	EN6a	2.3	1.18E-08	-	1.04E-06	1.12E-06	2.46E-06
EN7a	5.2	7.57E-03	EN7a	5.2	1.13E-07	2.74E-06	1.55E-05	1.60E-05	1.68E-05
EN8a	5.2	7.80E-03	EN8a	5.2	8.62E-09	-	1.48E-05	1.53E-05	1.59E-05
EN9a	6.4	1.25E-02	EN9a	6.4	3.84E-08	-	3.63E-05	5.25E-05	7.80E-05
EN10a	6.4	1.32E-02	EN10a	6.4	2.65E-07	-	2.53E-05	3.35E-05	6.06E-05
EN11a	6.4	8.71E-03	EN11a	6.4	1.84E-07	1.45E-06	1.34E-05	1.43E-05	2.42E-05
EN12b	7.5	6.13E-03	EN13a	9.9	5.43E-08	2.16E-07	2.01E-06	2.33E-06	1.21E-06
EN13a	9.9	−1.31E-03	EN15a	10.8	3.45E-08	3.77E-08	1.62E-07	1.87E-07	4.80E-07
EN14a	9.9	−1.12E-03	EN17a	12.5	1.13E-07	4.27E-07	5.39E-06	6.05E-06	1.26E-05
EN15a	10.8	−3.95E-03	EN18	12.5	1.13E-07	6.10E-07	5.65E-06	6.03E-06	1.15E-05
EN16a	10.8	−7.06E-03	EN20a	14.9	4.59E-08	2.47E-07	1.95E-06	2.39E-06	5.46E-06
EN17a	12.5	1.10E-03	EN21a	14.9	6.17E-08	3.12E-07	2.36E-06	3.02E-06	1.44E-05
EN18	12.5	2.48E-03	EN22a	15.8	5.80E-08	4.45E-07	3.78E-06	4.54E-06	1.84E-05
EN20a	14.9	−1.68E-03	EN23a	15.8	5.74E-08	5.28E-07	4.71E-06	6.15E-06	1.80E-05
EN21a	14.9	−1.55E-03	EN24a	17.5	8.87E-08	1.20E-06	9.11E-06	1.02E-05	1.60E-05
EN22a	15.8	−9.78E-04	EN25a	17.5	9.20E-08	1.20E-06	9.06E-06	1.05E-05	2.40E-05
EN23a	15.8	4.45E-04	EN26a	19.6	1.16E-07	1.19E-06	7.61E-06	1.16E-05	6.58E-05
EN24a	17.5	2.67E-03	EN27a	19.6	1.34E-07	1.39E-06	9.19E-06	1.47E-05	8.39E-05
EN25a	17.5	3.24E-03	EN28a	20.9	1.69E-07	6.87E-07	4.96E-06	1.86E-05	6.06E-05
EN26a	19.6	1.42E-03	EN29a	20.9	6.18E-08	4.11E-07	2.75E-06	4.55E-06	2.50E-05
EN27a	19.6	2.31E-03	EN30a	23.4	2.80E-07	3.12E-06	2.93E-05	3.09E-05	3.26E-05
EN28a	20.9	−5.93E-05	EN32a	24.7	9.76E-08	1.31E-06	1.25E-05	1.37E-05	1.61E-05
EN29a	20.9	−3.16E-03	EN33a	24.7	1.08E-07	1.12E-07	1.04E-05	1.14E-05	1.32E-05
EN30a	23.4	3.28E-03	EN34a	25	1.70E-07	1.98E-06	1.46E-05	1.55E-05	1.66E-05
EN31b	23.4	3.42E-03	EN35a	25	9.00E-08	7.98E-07	6.71E-06	9.69E-06	1.40E-05
EN32a	24.7	3.95E-03	EN36a	26.3	5.00E-08	5.12E-07	5.91E-06	6.83E-06	8.57E-06
EN33a	24.7	3.59E-03	EN37a	26.3	5.00E-08	4.62E-07	5.43E-06	6.25E-06	7.56E-06
EN34a	25	7.01E-03	EN39a	27.9	5.37E-07	1.30E-05	8.64E-05	8.90E-05	8.90E-05
EN35a	25	6.28E-03	EN40a	27.9	1.16E-07	1.52E-05	1.85E-04	1.92E-04	1.93E-04
EN36a	26.3	1.44E-03	EN41a	27.9	2.77E-06	9.93E-07	2.66E-04	2.78E-04	2.77E-04
EN37a	26.3	−4.23E-03	EN43a	30.9	1.51E-08	1.57E-07	1.67E-07	1.93E-07	4.12E-07
EN39a	27.9	1.70E-02	EN45a	32.4	3.59E-08	2.84E-07	4.25E-06	4.68E-06	7.52E-06
EN40a	27.9	2.26E-02	EN46a	35.6	4.74E-09	5.11E-08	3.94E-07	5.24E-07	9.84E-07
EN41a	27.9	2.38E-02	EN48a	37.5	5.66E-09	6.06E-08	4.33E-07	4.99E-07	1.22E-06
EN42a	30.3	1.11E-03	EN51a	39.6	4.34E-09	4.56E-08	5.74E-07	7.21E-07	1.21E-06
EN43a	30.9	−6.67E-04	EN52a	39.6	4.82E-09	5.06E-08	6.60E-07	8.35E-07	1.49E-06
EN45a	32.4	−7.05E-04	EN53a	40.6	3.51E-08	2.60E-07	3.08E-06	6.35E-06	6.19E-05
EN46a	35.6	−3.85E-03	EN55a	41.9	3.51E-08	1.33E-08	5.48E-06	6.41E-06	6.41E-07
EN47	35.6	−3.60E-03	EN58a	43.2	3.01E-08	2.21E-07	7.41E-06	8.32E-06	8.78E-06
EN48	37.5	−3.63E-03	EN59a	44.3	8.21E-09	7.60E-09	2.55E-06	2.96E-06	4.44E-06
EN48a	37.5	−3.72E-03	EN61a	45.3	3.79E-08	1.53E-07	2.35E-06	3.09E-06	7.57E-07
EN51a	39.6	−3.08E-03	EN64a	46.1	3.40E-08	1.49E-07	1.50E-06	1.65E-06	2.07E-06

(Continued)

TABLE 2 | Continued

(D) ENTREMÓN									
Site	**Position (m)**	**χ (m^3/kg)**	**Site**	**Position (m)**	**NRM (Am^2/kg)**	**ARM (Am2/kg)**	**SIRM (150 mT) (Am^2/kg)**	**SIRM (0.5 T) (Am^2/kg)**	**SIRM (1.8 T) (Am^2/kg)**
EN52a	39.6	−3.04E-03	EN66a	46.9	4.42E-08	2.71E-07	2.29E-06	2.47E-06	2.88E-06
EN53b	40.6	1.45E-03	EN71a	49	4.24E-08	1.41E-07	1.46E-06	1.66E-06	2.75E-06
EN55a	41.9	−7.13E-04	EN72a	49	1.11E-08	1.02E-07	1.80E-06	1.98E-06	2.31E-06
EN56a	41.9	9.87E-04	EN73a	49.7	3.36E-08	1.34E-07	1.56E-06	1.84E-06	2.71E-06
EN57a	43.2	4.97E-04	EN76a	50.6	3.71E-08	1.19E-07	1.05E-06	1.16E-06	1.60E-06
EN58a	43.2	−7.60E-04	EN77a	51.5	1.84E-08	2.58E-07	3.21E-06	3.54E-06	4.89E-06
EN59a	44.3	−1.17E-03	EN78a	51.5	4.43E-08	2.98E-07	1.11E-06	2.81E-06	5.63E-06
EN59b	44.3	−1.29E-03	EN104a	53.6	4.41E-08	2.43E-07	3.29E-06	3.83E-06	5.73E-06
EN60a	44.3	−1.25E-03	EN106a	54.1	1.00E-08	1.55E-07	2.30E-06	2.70E-06	4.00E-06
EN61a	45.3	−2.48E-03	EN108a	54.6	4.35E-08	2.01E-07	1.63E-06	1.97E-06	4.31E-06
EN62a	45.3	−3.54E-03	EN113a	55.9	8.60E-09	1.33E-07	1.84E-06	2.07E-06	2.13E-06
EN63a	46.1	−2.08E-03	EN114a	56.5	3.79E-08	1.44E-07	1.42E-06	1.63E-06	2.71E-06
EN64a	46.1	−2.21E-03	EN121a	57	4.22E-08	2.22E-07	2.42E-06	2.72E-06	3.43E-06
EN65a	46.9	−1.98E-03	EN123b	57.02	6.07E-09	1.02E-07	1.68E-06	2.12E-06	2.40E-06
EN66a	46.9	−1.30E-03	EN127a	57.3	7.34E-08	4.32E-07	4.10E-06	4.44E-06	6.23E-06
EN67a	47.7	−2.01E-03	EN130a	57.5	2.32E-08	5.13E-07	4.55E-06	4.88E-06	5.23E-06
EN69	48.8	−2.15E-03	EN131a	57.55	4.75E-08	5.14E-07	4.00E-06	4.26E-06	5.15E-06
EN71a	49	−2.00E-03	EN200base	57.7	7.41E-08	1.18E-06	2.51E-05	2.75E-05	2.90E-05
EN72a	49	−2.22E-03	EN200mid.	57.8	6.18E-08	1.28E-06	2.63E-05	2.87E-05	2.98E-05
EN73a	49.7	−1.89E-03	EN200top	57.9	1.48E-07	1.46E-06	2.26E-06	2.81E-05	2.68E-05
EN74a	49.7	−1.69E-03	EN134a	58.16	7.61E-08	1.28E-06	1.98E-05	2.10E-05	2.20E-05
EN76a	50.6	−1.69E-03	EN139	59.55	3.34E-08	1.13E-07	9.46E-07	1.25E-06	3.89E-06
EN76b	50.6	2.37E-04	EN141a	60.5	4.89E-09	5.35E-07	6.13E-06	6.54E-06	6.67E-06
EN77a	51.5	−1.75E-03	EN142a	60.5	1.96E-08	5.22E-07	6.82E-06	7.26E-06	7.67E-06
EN78a	51.5	−1.83E-03	EN146a	62	3.75E-08	9.63E-08	9.70E-07	1.43E-06	6.13E-06
EN100a	52.6	−2.48E-03	EN148a	62.9	6.68E-09	4.21E-08	7.02E-07	1.19E-06	4.02E-06
EN101a	52.7	−2.53E-03	EN149a	63.8	3.26E-08	6.66E-08	5.04E-07	7.86E-07	2.57E-06
EN102a	53.1	−1.45E-03	EN152a	64.8	3.72E-09	1.83E-07	3.08E-06	3.66E-06	5.48E-06
EN102b	53.1	−2.63E-03							
EN103a	53.1	−1.80E-03							
EN104a	53.6	−1.43E-03							
EN104b	53.6	−1.10E-03							
EN105a	53.6	3.70E-04							
EN105b	53.6	−2.94E-04							
EN106a	54.1	−1.50E-03							
EN108a	54.6	−1.83E-03							
EN109a	54.7	−2.05E-03							
EN110a	54.8	−2.13E-03							
EN111a	55.2	−1.77E-03							
EN112a	55.7	−2.32E-03							
EN113a	55.9	−2.59E-03							
EN113b	55.9	−2.28E-03							
EN114a	56.5	−1.99E-03							
EN115a	56.5	−2.14E-03							
EN116a	56.7	−1.81E-03							
EN117a	56.74	−1.61E-03							

(Continued)

TABLE 2 | Continued

(D) ENTREMÓN									
Site	**Position (m)**	**χ (m^3/kg)**	**Site**	**Position (m)**	**NRM (Am^2/kg)**	**ARM (Am2/kg)**	**SIRM (150 mT) (Am^2/kg)**	**SIRM (0.5 T) (Am^2/kg)**	**SIRM (1.8 T) (Am^2/kg)**
EN117b	56.74	−1.82E-03							
EN118a	56.75	−2.05E-03							
EN120a	56.9	−6.04E-04							
EN121a	57	−1.29E-03							
EN122a	57	−2.02E-03							
EN123b	57.02	−1.84E-03							
EN124a	57.15	−4.13E-04							
EN125a	57.2	−1.28E-03							
EN126a	57.2	−1.45E-03							
EN126b	57.2	−1.62E-03							
EN127a	57.3	−1.32E-03							
EN128a	57.4	−4.75E-04							
EN129a	57.4	−3.09E-04							
EN130a	57.5	−1.73E-03							
EN131a	57.55	−2.30E-04							
EN200base	57.7	3.92E-02							
EN200med	57.8	4.51E-02							
EN200top	57.9	2.83E-02							
EN132a	58.1	1.71E-02							
EN133a	58.16	2.05E-02							
EN134a	58.16	1.68E-02							
EN135a	58.26	−2.23E-03							
EN136a	58.7	−1.92E-03							
EN138a	59	−1.96E-03							
EN139	59.55	−3.10E-03							
EN140a	59.6	−2.90E-03							
EN141a	60.5	5.04E-04							
EN142a	60.5	2.10E-03							
EN142b	60.5	2.27E-03							
EN142c	60.5	3.38E-03							
EN143a	61.1	−2.44E-03							
EN144a	61.15	−3.20E-03							
EN145a	62	−2.49E-03							
EN146a	62	−2.14E-03							
EN147a	62.9	−2.28E-03							
EN148a	62.9	−2.78E-03							
EN149a	63.8	−3.63E-03							
EN150a	63.8	−3.25E-03							
EN150b	63.8	−2.67E-03							
EN151a	64.8	−2.92E-03							
EN152a	64.8	−4.41E-03							
EN152b	64.8	−3.04E-03							

*2**(A)** Carriata, 2**(B)** Bujaruelo, 2**(C)** Gallisué, and 2**(D)** Entremón. Name of sites, positions, and values of magnetic susceptibility (χ), NRM, ARM, SIRM (at different values) and SIRM (at 0.5 mT)/ ARM, and coercivity of the remanence (only for Gallisué section). All values are normalized by mass.*

Mondarruego Fm are sandy limestones which undergo transition to bioclastic limestones with corals located at ∼45 m from the base of the section. Dolostones are found in the upper part of the Mondarruego Fm. The San Úrbez Fm is mostly represented by sandy limestones and dolostones with parallel and cross bedding. The boundary between the Paleocene-Ilerdian was karstified (see **Figure 4B**). The Góriz Fm is formed by limestones and limestones with chert nodules at the top. Cleavage due to pressure solution parallel and perpendicular to bedding is found in the whole section, particularly in the fine-grained rocks.

In the Entremón section, limestones from the Mondarruego Fm, sandy limestones from the San Úrbez, and La Pardina Fms were sampled. However, the Faja de las Flores Mb is not present, as it occurs in the Gallisué section. The Paleocene-Ilerdian boundary is sharp and marked by a thin layer of abiotic gray marls (∼30 cm) located at 60 m from the base of the section (**Figure 5**). Some intervals within the limestones and sandy limestones show red-brownish color. These intervals also correspond to the presence of *Microcodium* due to low sea level (Pujalte et al., 2016).

Rock Magnetic Minerals

The thermomagnetic curves inform about the type of magnetic mineral present in the samples since every mineral has a diagnostic temperature over which the ferromagnetic behavior changes to paramagnetic (Curie or Néel temperature, Dunlop and Özdemir, 1997 and references therein). The selected samples show irreversible thermomagnetic curves. The heating produces a generation of magnetite in all analyzed samples (see the increase of the magnetization during heating after 450°C). This behavior is observed in the Faja de las Flores Mb, La Pardina Fm (EN201), and Góriz Fm (GA208. EN142c) samples (**Figure 6a**). The presence of magnetite is recognized by the main decay of the induced magnetization at 580°C (Curie temperature of magnetite). The heating curves do not completely flatten after 580°C (except for the Bujaruelo sample), suggesting the presence of high coercivity minerals. This creation of new magnetite during heating is found in, for example, samples where iron contained in the biotite transforms to the ferromagnetic in magnetite during heating (Trindade et al., 2001). In addition, iron oxides can be formed from other minerals such as iron sulfides (pyrite, pyrrhotite, greigite, and troilite), carbonates (siderite and ankerite), silicates, and other iron oxides or hydroxides (e.g., Schwartz and Vaughan, 1972; Dekkers, 1990a,b). The small indentation in the cooling curves of Bujaruelo section (Faja de las Flores Mb) and in the abiotic gray marl of the Entremón section at about 300°C may suggest the presence of pyrrhotite (Curie temperature of ∼325°C masked in the heating curve by the large peak of the secondary magnetite). However, the enlargement of the heating curve does not show any inflection around 325°C. The acquisition of the IRM (**Figure 6b**) shows that the samples saturate above 0.6 T (except sample GA134), indicating the presence of a low coercivity mineral. The values of the coercivity of the remanence are below 70 mT except for few samples in the Gallisué section (**Table 2C**). Hysteresis loops performed in a MMVFTB reveal the presence of a low coercivity mineral even though the samples are weak and do not close at high fields (**Figure 6c**).

Paleomagnetic Directional Analyses

Thermal demagnetization diagrams are shown in **Figure 7** and **Supplementary Table 1**. The decay of the remanence with temperature shows a main decay at 200–300°C except for MON4a, where the main decay of the remanence occurs at 100°C. Afterwards, the remanence increases and decreases again and becomes zero /or erratic between ∼450°–500° and 600°C. **Table 1** groups the characteristic with paleomagnetic components calculated between 300–325°C and 400–450°C or between 40 mT and 80 mT for each of the three northern sections. In Gallisué section, data were grouped along the section in 9 groups. The characteristic component is always the reverse in the three northern sections and it does not always direct toward the origin; therefore, it is anchoring to the line-fit without considering the origin of the diagram. In Entremón section, the magnetization is unstable and only a characteristic component between 140° or 250° and 460° or 540°C has been calculated in 6 samples (out of 31). The component does not have a common direction either in geographic or in tilt-corrected setting. Therefore, a robust average cannot be calculated.

Fold Test

A classical fold test is performed for the characteristic reverse component calculated in the three northern sections and an Upper Cretaceous site in Añisclo valley (**Table 1**). The fold test is negative and it reveals that the stable characteristic component is acquired after the beds were tilted during a period of reverse magnetic field (**Figure 8**).

Rock Magnetic Properties

Bulk magnetic susceptibility values normalized by mass (χ) range from 0.01 E-6 m^3/kg to 1.2 E-6 m^3/kg (**Figures 9**, **10**, **Tables 2A–D**). The highest values occur in the Faja de las Flores Mb in the Carriata and Bujaruelo sections. In Entremón, the highest values of the magnetic susceptibility coincide with the abiotic marly interval of the onset of Ilerdian sedimentation. The negative values of the bulk magnetic susceptibility correspond to the predominance of diamagnetic behavior related to the predominance of calcite (diamagnetic mineral) and low content of paramagnetic (phyllosilicates) and ferromagnetic minerals (for example, magnetite). The saturation of Isothermal Remanent Magnetization at 0.5 T varies from 3.66 E-4 Am^2/kg to 2 E-6 Am^2/kg in Carriata section. A linear relationship between SIRM and ARM values is found in the three measured sections of Carriata, Bujaruelo, and Entremón (**Figure 11**), suggesting that an increase in concentration of ferromagnetic minerals relates to higher SIRM and ARM. The highest value of ARM occurs in Carriata (1.91 E-5 Am^2/kg) at the top of the San Úrbez Fm (**Figure 9**) and the lowest value is 4 E-9 Am^2/kg. Different saturation fields for the SIRM analyses were applied in different sections. The saturation field of 0.5 T was applied to all sections.

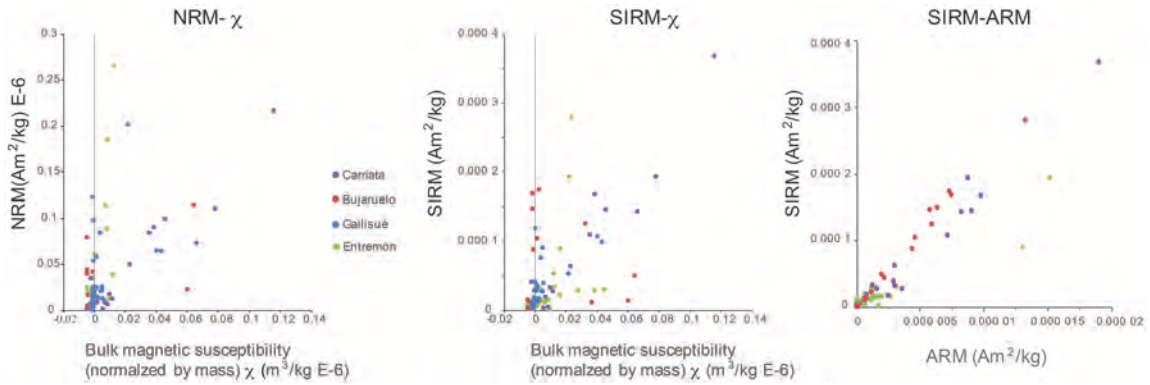

FIGURE 11 | Biplot diagrams with magnetic values of NRM, bulk susceptibility, SIRM (at 0.5 T), and ARM, normalized by mass.

In addition, the Bujaruelo samples were subjected to 1.9 T field and the Entremón samples to 150 mT and 1.8 T fields.

The magnetic signal of the NRM, ARM, and SIRM of the two northern sections increases concomitantly with the magnetic susceptibility suggesting that the ferromagnetic content increases. The increase occurs before the onset of the PETM (Faja de las Flores Mb). In the Bujaruelo section, the SIRM was also applied using 0.5 T and 0.9 T fields. The similar values of the remanent magnetization for the two applied fields indicate that no high coercitive minerals (such as hematite or goethite, known as "hard" magnetic minerals) are present.

In the southern sections, where La Pardina Fm (onset of PETM) is not present, the magnetic signal also varies, particularly in the Entremón section, where three peaks in the magnetic properties measured are visible: two in the Mondarruego Fm and one at the beginning of the Ilerdian, strictly related to an abiotic marly interval (gray bars in **Figure 10**).

The magnetic signal in Gallisué relates to the low content of ferromagnetic (and paramagnetic) minerals in the carbonatic rocks, particularly seen in the abundance of negative values of the magnetic susceptibility. The coercivity of remanence values measured in this part of the section have an average of −66 mT with higher values in the gray bar (not shown in **Figure 9**), suggesting the presence of mineral with high coercivity in such interval.

The magnetic signal in Entremón shows three "excursions" or higher values (positive excursions marked with gray bars in **Figure 10**). Looking at the SIRM column, the "excursion" of the upper part of the section shows similar values for the three SIRMs, therefore, indicating the presence of low coercivity minerals such as magnetite. However, in the two lower intervals or "excursions" with higher magnetic property values, the SIRM increases with increasing magnetic fields suggesting the presence of high coercivity minerals (hematite, goethite).

The variation of the SIRM/ARM ratio in the three analyzed sections remains fairly constant. This ratio is related to the magnetic mineralogy grain size when the mineralogy remains constant (Peters and Dekkers, 2003), therefore, indicating that the magnetic signal increase at certain depths is not related to magnetic grain size variations, but to the ferromagnetic mineral concentration.

DISCUSSION

Positive Excursion of the Magnetic Signal

The magnetic signal of rocks has been useful to determine the position of the PETM interval in lithologically more homogeneous sections in New Zealand (Villasante-Marcos et al., 2009). In the southwest-central Pyrenees, the marine sediments of the PETM record a large "excursion" in the magnetic properties during the PETM interval in Carriata and Bujaruelo sections. The "excursion" is localized around a marly interval (Faja de las Flores Mb) and neighboring limestones. The Faja de las Flores Mb has been interpreted as the prodelta sedimentation related to the climatic change of the PETM due to an intensification of the hydrological cycle with a previous lowering of the sea level (Pujalte et al., 2016 and references therein). The Paleocene-Eocene lithology in the SW Pyrenees is not as homogeneous as the lithology of New Zealand. However, it is noticeable that the increase of the bulk magnetic susceptibility values is up to two orders of magnitude of Faja de las Flores Mb in the two northern sections. In addition, the increase of the magnetic susceptibility (and the values of the other magnetic properties, **Figure 9**) predates the onset of the marly sediments. This indicates an increase in the content of ferromagnetic minerals prior to the lithological change linked to the onset of the PETM, and a subsequent decrease during the marly sediments. After the marly interval of Faja de las Flores Mb, limestones displayed unexpected (for their lithological type) higher magnetic values. Generally, marls and marly limestones show higher values of, magnetic susceptibility than limestones: standard bulk magnetic susceptibility is ∼200 SI in marls and it can reach negative values in limestones due to the predominance of calcite as diamagnetic mineral (Borradaile and Jackson, 2004 and references therein).

The SIRM/ARM ratio indicates the variation of magnetic grain size when magnetic mineralogy is homogeneous throughout the sampled section. The dispersion of the

SIRM/ARM remains approximately consistent throughout the sections, suggesting a similar grain-size distribution. On the other hand, the good correlation of the curve of ARM and SIRM also suggests a uniform grain-size distribution of the low coercivity mineral (as also seen in Hirt et al., 2003). In addition, the concomintant increase in χ, ARM, and SIRM values during the PETM ("magnetic properties excursion") indicates that the ferromagnetic content of the samples increases not only in the Faja de las Flores Mb (marly interval), but also in the neighboring limestones in the two northern sections (Carriata and Bujaruelo). Magnetite has low coercivity values (and it is typically referred as "soft"), and it would be saturated at low fields (typically, magnetite saturates below 0.5 T), whereas hematite or goethite have high coercivity values ("hard") and they are not saturated by the maximum fields (of 1.9 T) applied in this study. The increase of the ferromagnetic content in the Bujaruelo section is related to magnetite since the values of SIRM at 0.5 T and 1.9 T magnetic fields give similar results.

However, the presence of a positive magnetic signal excursion is not diagnostic of the PETM. In the southernmost sections (particularly in the Entremón section), there is no record of the PETM due to the regression of the ocean coast toward the North (Robador et al., 2009; Pujalte et al., 2016). Nevertheless, the magnetic signal increases at certain intervals. In the Entremón section, the peak of the magnetic signal coincides with an abiotic marly layer and it is strictly constrained to the marly interval (neighboring limetones show no excursion), which was expected due to change in lithology. Below, in the first 30 m of the section, there is a wide distribution of magnetic properties that are not observed in the northernmost sections. The increase in the SIRM values at increasing magnetic field values in the lower part of the Entremón section, particularly, in the magnetic excursions marked with gray bars in **Figure 10**, suggests the presence of high coercivity minerals in those intervals of sandy limestones.

Origin of Magnetite in the PETM of the SW Pyrenees

The origin of magnetite, detrital, diagenetic, or biogenetically induced cannot be deduced directly from the data presented here, but since La Pardina Fm is related to the expansion of a braid delta toward the North (Pujalte et al., 2016), it seems plausible to infer tentatively a detrital origin for the abundance of primary magnetite in the marly interval (Faja de las Flores Mb at the bottom of La Pardina Fm) with respect to the limestones of the carbonate platform. An abrupt increase in the discharge and sediment supply of rivers has been deduced in the Carriata/Bujaruelo sections area, since a 10 km progradation of the delta of La Pardina Fm has been inferred in the short time of the PETM duration (Pujalte et al., 2016). In addition, recent compilations suggest that at middle latitudes, the lithologic, or sedimentologic changes associated with the PETM hydrological perturbation were more dramatic (Pujalte et al., 2016 and references therein).

However, the alpine deformation and the construction of the Pyrenean orogeny have produced remagnetization events recorded by magnetite. Remagnetizations have been described in the carbonatic materials of the Upper Cretaceous and part

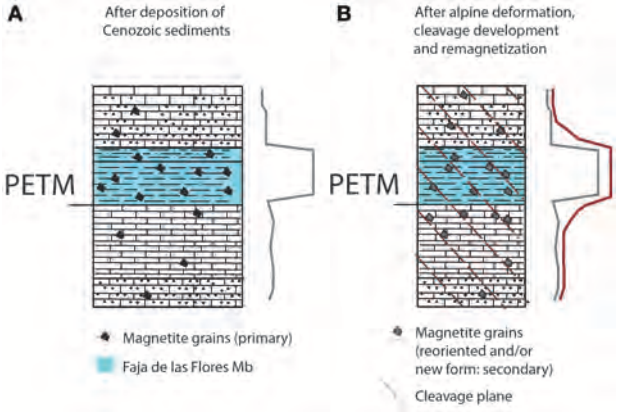

FIGURE 12 | Sketch of the concentration of magnetite grains (profile on the right of every column). **(A)** After deposition of the Cenozoic rocks (primary) in gray and **(B)** after alpine deformation cleavage development due to pressure solution and remagnetization (due to reorientation and new formation of magnetite—secondary —) in red.

of the Eocene rocks (Oliva-Urcia and Pueyo, 2007; Oliva-Urcia et al., 2008; Izquierdo-Llavall et al., 2015). In addition, the new paleomagnetic data of the three northernmost sections also reveal the presence of the post-folding remagnetization component, confirming a secondary magnetite production during the pyrenean deformation.

The tectonic-sedimentary load and the pressure solution cleavage development associated to that load during the Pyrenean deformation have facilitated the reorganization of the original magnetite and probably its new formation at different stages of the orogeny's evolution, since remagnetization events are recorded by magnetite (Oliva-Urcia et al., 2008; Izquierdo-Llavall et al., 2015). The cleavage development during the Pyrenean orogeny produces the dissolution of carbonatic material and the remobilization of those fluids, leaving the insoluble material (iron oxides among it) concentrated in microlithons (Holl and Anastasio, 1995; Oliva-Urcia et al., 2008). This pressure solution event explained, at first, the post-folding remagnetization found in the Upper Cretaceous (Oliva-Urcia et al., 2008). The same post-folding remagnetization is found in the analyzed materials around the PETM interval in the three northern sections of this study.

According to Lacroix et al. (2014), the pressure-solution cleavage was associated with calcite-quartz shear and extension veins. The geochemistry analyses performed on those veins indicate that a local fluid-assisted mass transfer from the sediment to the veins does not necessitate large fluid flow. These apparently closed hydrological fluid flow systems in combination with the cleavage development may have produced the remobilization and the reorientation of the primary ferromagnetic minerals (Oliva-Urcia et al., 2008) and the new formation of the ferromagnetic minerals from the Faja de las Flores Mb to the adjacent rocks, as it has been deduced in the Upper Cretaceous rocks (Izquierdo-Llavall et al., 2015). This supposition would explain that the magnetic signal excursion is observed, not only constrained to the marly interval of the Faja

de las Flores Mb, but also in the limestones neighboring the Faja de las Flores Mb, about 10 m in the Carriata section and <5 m in the Bujaruelo section, below the onset of the Faja de las Flores Mb and above the end of the Faja de las Flores Mb (**Figures 9**, **12**).

The cleavage development affecting the three northernmost sections is mainly related to the Gavarnie basement thrust (Teixell, 1992). In addition, it has been calculated that the Carriata section has been transported toward the south at least 10 km more than the Bujaruelo section due to the Larra-Monte Perdido thrust system (see geological location above), which was active prior to the Gavarnie basement thrust (Teixell, 1992, 1996; Millán Garrido et al., 2006).

In the southernmost section (Entremón), the excursion of the magnetic signal around the PETM interval is related to a "soft" coercivity mineral (magnetite), as increasing magnetic fields provide similar values of SIRMs (**Figure 10**) and it is strictly confined to the abiotic marly interval. This Entremón section is out of the cleavage front (Izquierdo-Llavall et al., 2013) and, therefore, neither pressure solution cleavage development nor closed hydrological fluid flow is occurring in the section during the Pyrenean deformation. The sedimentation in this section indicates low sea level interval and shallow marine environments during Mondarruego and San Úrbez Fms deposition. The magnetic excursions taking place in the Mondarruego and the San Úrbez Fms in sandy limestones intervals (gray bars in **Figure 10**) are most probably associated to the presence of other ferromagnetic minerals since the SIRM values at higher magnetic fields increase the magnetic signal. Therefore, high coercivity minerals (hematite and/or goethite) are possibly present, as it is also suggested by the thermomagnetic curves. These intervals may be associated with different oxidation conditions due to the low sea level and the occurrence of subaerial exposures on this part of the studied area during the PETM period.

CONCLUSIONS

The PETM has been widely studied for the effects of the release of light carbon into the atmosphere and the rise of ocean (surficial and deep) and terrestrial temperatures. This is due to the similarities observed in the present worldwide rise of average temperatures (McInerney and Wing, 2011). Magnetic properties can be a proxy to detect past environmental changes.

Increases in magnetic values (magnetic excursions) are observed in the four studied sections. In the two northern sections, these excursions are interpreted to be "derived" from the primary magnetic signal during the PETM. The primary magnetic signal in the SW Pyrenees produced higher magnetic signal in marls than in limestones in relation to the enhancement of the hydrological system during the PETM. This primary magnetic signal is modified during the alpine deformation (transformed to new formation/rotation of ferromagnetic minerals). Therefore, the derived enhanced magnetic signature of the PETM sediments (Faja de las Flores Mb) in the two northern sections is due to the Pyrenean deformation, which produces cleavage development and a close hydrological fluid flow system. In this situation, the Pyrenean deformation could produce an increase in the magnetite content of the neighboring rocks of the Faja de las Flores Mb as it is observed in the Carriata and Bujaruelo sections.

In the southernmost section, the magnetic signature is related to the naturally higher content of magnetite in marls (the abiotic gray marl interval in Entremón section) than in limestones and most probably due to the presence of different magnetic mineralogies (soft and hard: magnetite and hematite) in the red-brownish limestones and sandy limestones due to different oxidation conditions when in low sea level/subaerial intervals. Nowadays, magnetic excursion found around the PETM interval in the SW Pyrenees is related to lithologically contrasted marls/limestones. In the two northern sections, a modification of the ferromagnetic content in the neighboring limestones of the marly interval recording of the PETM is interpreted to be related to the Pyrenean deformation and cleavage development.

AUTHOR CONTRIBUTIONS

All authors have contributed to sampling. Field work was carried out by BO-U, IG-P, RS and JMS. Analyses were performed by BO-U. Writing, figures, and tables were created by BO-U with revisions from the rest of the authors. Discussions about the structure, data display and content leading to the final manuscript were carried out by BO-U, IG-P, IR, RS and JMS.

ACKNOWLEDGMENTS

Thanks for the financial support from the Autonomous Organism of National Parks for the project 074/2006 (Principal Researcher A. Robador) and the Sobrarbe Geopark (now Sobrarbe-Pyrenees UNESCO World Geopark) for their financial support to the MAXTERMAG project. Reviewers are acknowledged for their detailed and helpful comments that contributed to improve the first version of the manuscript. Editor L. Jovane is acknowledged for helping in the handling of the manuscript.

SUPPLEMENTARY MATERIAL

The Supplementary Material for this article can be found online at: https://www.frontiersin.org/articles/10.3389/feart.2018.00202/full#supplementary-material

REFERENCES

Aziz, H. A., Hilgen, F. J., van Luijk, G. M., Sluijs, A., Kraus, M. J., Pares, J. M. et al. (2008). Astronomical climate control on paleosol stacking patterns in the upper Paleocene–lower Eocene Willwood Formation, Bighorn Basin, Wyoming. *Geology* 36, 531–534. doi: 10.1130/G24734A.1

Baceta, J., Pujalte, V., Wright, V. P., and Schmitz, B. (2011). "Carbonate platform models, sea-level changes and extreme climatic events during the Paleocene-early Eocene greenhouse interval: a basin-platform-coastal plain transect across the southern Pyrenean basin," in *Pree-Meeting Field trips Guidebook, 28th IAS Meeting*, eds C. Arenas, L. Pomar, and F. Colombo, (Zaragoza: Sociedad Geológica de España, Geo-Guías), Vol. 7, 151–198.

Baceta, J. I., Pujalte, V., Serra-Kiel, J., Robador, A., and Orue-Etxebarria, X. (2004). "El Maastrichtiense final, Paleoceno e Ilerdiense inferior de la Cordillera Pirenaica," in *Geología de España Sociedad Geológica de España-Instituto Geológico y Minero de España*, ed J. A. Vera (Madrid), 308–313.

Barnolas, A., and Gil-Peña, I. (2001). Ejemplos de relleno sedimentario multiepisódico en una cuenca de antepaís fragmentada: La Cuenca Surpirenaica. *Boletín Geol. Minero* 112, 17–38.

Beamud, E., Muñoz, J. A., Fitzgerald, P. G., Baldwin, S. L., Garcés, M., Cabrera, L., et al. (2011). Magnetostratigraphy and detrital apatite fission track thermochronology in syntectonic conglomerates: constraints on the exhumation of the South-Central Pyrenees. *Basin Res.* 23, 309–331. doi: 10.1111/j.1365-2117.2010.00492.x

Bentham, P. A. (1992). *The tectono-Stratigraphic Development of the Western Oblique Ramp of the South-Central Pyrenean Thrust System, Northern Spain*. Ph.D. University of Southern California.

Borradaile, G. J., and Jackson, M. (2004). Anisotropy of magnetic susceptibility (AMS): magnetic petrofabrics of deformed rocks. *Geol. Soc. Lond. Spec. Publ.* 238, 299–360. doi: 10.1144/GSL.SP.2004.238.01.18

Bowen, G. J., Bralower, T. J., Delaney, M. L., Dickens, G. R., Kelly, D. C., Koch, P. L., et al. (2006). Eocene hyperthermal event offers insight into greenhouse warming. *Eos Trans. Am. Geophys.* 87, 165–169. doi: 10.1029/2006EO170002

Bowen, G. J., Clyde, W. C., Koch, P. L., Ting, S., Alroy, J., Tsubamoto, T., et al. (2002). Mammalian dispersal at the Paleocene/Eocene boundary. *Science* 295, 2062–2065. doi: 10.1126/science.1068700

Bowen, G. J., Maibauer, B. J., Kraus, M. J., Röhl, U., Westerhold, T., Steimke, A., et al. (2015). Two massive, rapid releases of carbon during the onset of the Palaeocene–Eocene thermal maximum. *Nat. Geosci.* 8:44. doi: 10.1038/ngeo2316

Chadima, M., and Hrouda, F. (2007). *Remasoft 3.0: Paleomagnetic Data Browser and Analyzer*.

Charles, A. J., Condon, D. J., Harding, I. C., Pälike, H., Marshall, J. E., Cui, Y., et al. (2011). Constraints on the numerical age of the Paleocene-Eocene boundary. *Geochem. Geophys. Geosyst.* 12, 1–19. doi: 10.1029/2010GC003426

Choukroune, P., Martinez, C., Seguret, M., and Mattauer, M. (1968). Sur L'extension, le Style et l'sge de Mise en place de la Nappe de Gavarnie (Pyrenees centrales). *Compres Rendus de 1'Acad. des Sci.* 260, 1360–1363.

Choukroune, P., and Séguret, M. (1973). *Carte Structurale des Pyrénées*. ELF-ERAP. Mission France, Boussens.

Clyde, W. C., and Gingerich, P. D. (1998). Mammalian community response to the latest Paleocene thermal maximum: an isotaphonomic study in the northern Bighorn Basin, Wyoming. *Geology* 26, 1011–1014.

Cramer, B. S., and Kent, D. V. (2005). Bolide summer: the Paleocene/Eocene thermal maximum as a response to an extraterrestrial trigger. *Palaeogeogr. Palaeoclimatol. Palaeoecol.* 224, 144–166. doi: 10.1016/j.palaeo.2005.03.040

Dekkers, M. J. (1990a). Magnetic monitoring of pyrrhotite alteration during thermal demagnetisation. *Geophys. Res. Lett.* 17, 779–782. doi: 10.1029/GL017i006p00779

Dekkers,. M. J. (1990b). Magnetic properties of natural goethite—III. Magnetic behaviour and properties of minerals originating from goethite dehydration during thermal demagnetisation. *Geophys. J. Int.* 103, 233–250.

Dickens, G.R. (1999). Carbon cycle: the blast in the past. *Nature* 401:752.

Dickens, G. R. (2008). Palaeoclimate: the riddle of the clays. *Nat. Geosci.* 1:86. doi: 10.1038/ngeo118

Drobne, K., JeŽ, J., Cosović, V., Ogorelec, B., Stenni, B., and Zakrevskaya, E. (2014). "Identification of the Palaeocene–Eocene Boundary based on larger foraminifers in deposits of the Palaeogene Adriatic Carbonate Platform, southwestern Slovenia," in *STRATI 2013* (Cham: Springer), 89–93.

Dunlop, D. J. (1972). Magnetic mineralogy of unheated and heated red sediments by coercivity spectrum analysis. *Geophys. J. Int.* 27, 37–55. doi: 10.1111/j.1365-246X.1972.tb02346.x

Dunlop, D. J., and Özdemir, Ö. (1997). *Rock Magnetism, Fundamentals and Frontiers. Cambridge Studies in Paleomagnetism*. (Cambridge, New York, NY: Cambridge Studies in Magnetism Series), xxi–573.

Farley, K. A., and Eltgroth, S. F. (2003). An alternative age model for the Paleocene–Eocene thermal maximum using extraterrestrial 3 He. *Earth Planet. Sci. Lett.* 208, 135–148. doi: 10.1016/S0012-821X(03)00017-7

Fernández, O., Muñoz, J. A., Arbués, P., and Falivene, O. (2012). 3D structure and evolution of an oblique system of relaying folds: the Ainsa basin (Spanish Pyrenees). *J. Geol. Soc. London* 169, 545–559. doi: 10.1144/0016-76492011-068

Foreman, B. Z., Heller, P. L., and Clementz, M. T. (2012). Fluvial response to abrupt global warming at the Palaeocene/Eocene boundary. *Nature* 491:92. doi: 10.1038/nature11513

Gibbs, S. J., Bown, P. R., Sessa, J. A., Bralower, T. J., and Wilson, P. A. (2006). Nannoplankton extinction and origination across the Paleocene-Eocene thermal maximum. *Science* 314, 1770–1773. doi: 10.1126/science.1133902

Gibson, T. G., Bybell, L. M., and Mason, D. B. (2000). Stratigraphic and climatic implications of clay mineral changes around the Paleocene/Eocene boundary of the northeastern US margin. *Sediment. Geol.* 134, 65–92. doi: 10.1016/S0037-0738(00)00014-2

Gingerich, P. D. (2003). "Mammalian responses to climate change at the Paleocene-Eocene boundary: Polecat Bench record in the northern Bighorn Basin," in *Special Papers*, (Geological Society of America), 463–478.

Hirt, A. M., Lanci, L., and Koinig, K. (2003). Mineral magnetic record of Holocene environmental changes in Sägistalsee, Switzerland. *J. Paleolimnol.* 30, 321–331. doi: 10.1023/A:1026028728241

Holl, J. E., and Anastasio, D. J. (1995). Cleavage development within a foreland fold and thrust belt, southern Pyrenees, Spain. *J. Struct. Geol.* 17, 357–369. doi: 10.1016/0191-8141(94)00062-5

Hunt, C. P., Banerjee, S. K., Han, J., Solheid, P. A., Oches, E., Sun, W., et al. (1995). Rock-magnetic proxies of climate change in the loess-palaeosol sequences of the western Loess Plateau of China. *Geophys. J. Int.* 123, 232–244. doi: 10.1111/j.1365-246X.1995.tb06672.x

Izquierdo-Llavall, E., Aldega, L., Cantarelli, V., Corrado, S., Gil-Peña, I., Invernizzi, C., et al. (2013). On the origin of cleavage in the Central Pyrenees: structural and paleo-thermal study. *Tectonophysics* 608, 303–318. doi: 10.1016/j.tecto.2013.09.027

Izquierdo-Llavall, E., Sainz, A. C., Oliva-Urcia, B., Burmester, R., Pueyo, E. L., and Housen, B. (2015). Multi-episodic remagnetization related to deformation in the Pyrenean Internal Sierras. *Geophys. J. Int.* 201, 891–914. doi: 10.1093/gji/ggv042

Jaramillo, C., Rueda, M. J., and Mora, G. (2006). Cenozoic plant diversity in the Neotropics. *Science* 311, 1893–1896. doi: 10.1126/science.1121380

Kelly, D. C., Bralower, T. J., Zachos, J. C., Silva, I. P., and Thomas E. (1996), Rapid diversification of planktonic foraminifera in the tropical Pacific (ODP Site 865) during the late Paleoecene thermal maximum, *Geology* 24, 423–426. doi: 10.1130/0091-7613(1996)024<0423:RDOPFI>2.3.CO;2.

Kelly, D. C., Zachos, J. C., Bralower, T. J., and Schellenberg, S. A. (2005). Enhanced terrestrial weathering/runoff and surface ocean carbonate production during the recovery stages of the Paleocene-Eocene thermal maximum. *Paleoceanography* 20:PA4023. doi: 10.1029/2005PA001163

Kennett, J. P., and Stott, L. D. (1991). Abrupt deep-sea warming, palaeoceanographic changes and benthic extinctions at the end of the Palaeocene. *Nature* 353:225. doi: 10.1038/353225a0

Kent, D. V., Cramer, B. S., Lanci, L., Wang, D., Wright, J. D., and Van der Voo, R. (2003). A case for a comet impact trigger for the Paleocene/Eocene thermal maximum and carbon isotope excursion. *Earth Planet. Sci. Lett.* 211, 13–26. doi: 10.1016/S0012-821X(03)00188-2

Kirschvink, J. L. (1980). The least-squares line and plane and the analysis of paleomagnetic data. *Geophys. J. Int.* 62, 669–718. doi: 10.1111/j.1365-246X.1980.tb02601.x

Koch, P. L., Zachos, J. C., and Gingerich, P. D., (1992). Correlation between isotopic records in marine and continental reservoirs near the Paleocene/Eocene boundary. *Nature* 358, 319–322. doi: 10.1038/358319a0

Kopp, R. E., Raub, T. D., Schumann, D., Vali, H., Smirnov, A. V., and Kirschvink, J. L. (2007). Magnetofossil spike during the Paleocene-Eocene thermal maximum: ferromagnetic resonance, rock magnetic, and electron microscopy evidence from Ancora, New Jersey, United States. *Paleoceanography* 22, 9–16. doi: 10.1029/2007PA001473

Kopp, R. E., Schumann, D., Raub, T. D., Powars, D. S., Godfrey, L. V., Swanson-Hysell, N. L., et al. (2009). An appalachian amazon? magnetofossil evidence for the development of a tropical river-like system in the mid-atlantic united states during the Paleocene-eocene thermal maximum. *Paleoceanography* 24, 65–82. doi: 10.1029/2009PA001783

Labaume, P., Meresse, F., Jolivet, M., Teixell, A., and Lahfid, A. (2016). Tectonothermal history of an exhumed thrust-sheet-top basin: an example from the south Pyrenean thrust belt. *Tectonics* 35, 1280–1313. doi: 10.1002/2016TC004192

Labaume, P., Séguret, M., and Seyve, C. (1985). Evolution of a turbiditic foreland basin an analogy with an accretionary prism: example of the Eocene South-Pyrenean basin. *Tectonics* 4, 661–685. doi: 10.1029/TC004i007p00661

Lacroix, B., Travé, A., Buatier, M., Labaume, P., Vennemann, T., and Dubois, M. (2014). Syntectonic fluid-flow along thrust faults: example of the South-Pyrenean fold-and-thrust belt. *Mar. Petrol. Geol.* 49, 84–98. doi: 10.1016/j.marpetgeo.2013.09.005

Lee, Y. S., and Kodama, K. (2009). A possible link between the geomagnetic field and catastrophic climate at the Paleocene-Eocene thermal maximum. *Geology* 37, 1047–1050. doi: 10.1130/G30190A.1

Lippert, P. C., Zachos, J., Bohaty, S., and Quattlebaum, T. (2004). *Rock Magnetic Properties Across Paleocene-Eocene boundary Sediments from the North Atlantic, South Atlantic, and Eastern Pacific.* AGU Fall Meeting Abstracts.

Lippert, P. C., and Zachos, J. C. (2007). A biogenic origin for anomalous fine-grained magnetic material at the Paleocene-Eocene boundary at Wilson Lake, New Jersey. *Paleoceanography* 22:PA4104. doi: 10.1029/2007PA001471

Luterbacher, H., Hardenbol, J., and Schmitz, B. (2000). Decision of the voting members of the International Sub-commission on Paleogene Stratigraphy on the criterion for the recognition of the Paleocene/Eocene boundary. *Newsl. Int. Subcomm. Paleogene Stratigr.* 9:13.

Martinez-Peña, M., and Casas-Sainz, A. (2003). Cretaceous–Tertiary tectonic inversion of the Cotiella Basin (southern Pyrenees, Spain). *Int. J. Earth Sci.* 92, 99–113. doi: 10.1007/s00531-002-0283-x

McElhinny, M. W. (1964). Statistical significance of the fold test in palaeomagnetism. *Geophys. J. Int.* 8, 338–340. doi: 10.1111/j.1365-246X.1964.tb06300.x

McFadden, P. L. (1990). A new fold test for palaeomagnetic studies. *Geophys. J. Int.* 103, 163–169. doi: 10.1111/j.1365-246X.1990.tb01761.x

McInerney, F. A., and Wing, S. L. (2011). The Paleocene-Eocene Thermal Maximum: a perturbation of carbon cycle, climate, and biosphere with implications for the future. *Annu. Rev. Earth Planet. Sci.* 39, 489–516. doi: 10.1146/annurev-earth-040610-133431

Millán Garrido, H., Oliva Urcia, B., and Pocoví Juan, A. (2006). La transversal de GavarnieGuara. Estructura y edad de los mantos de Gavarnie. Guara-Gèdre y Guarga (Pirineo centro-occidental). *Geogaceta* 40, 35–38.

Mochales, T., Casas, A. M., Pueyo, E. L., and Barnolas, A. (2012). Rotational velocity for oblique structures (Boltaña anticline, Southern Pyrenees). *J. Struct. Geol.* 35, 2–16. doi: 10.1016/j.jsg.2011.11.009

Muñoz, J. A. (1992). "Evolution of a continental collision belt: ECORS-Pyrenees crustal balanced cross-section," in *Thrust tectonics*, ed K. R. McClay (Dordrecht: Springer), 235–246.

Muñoz, J. A., Beamud, E., Fernández, O., Arbués, P., Dinarès-Turell, J., and Poblet, J. (2013). The Ainsa Fold and thrust oblique zone of the central Pyrenees: kinematics of a curved contractional system from paleomagnetic and structural data. *Tectonics* 32, 1142–1175. doi: 10.1002/tect.20070

Murphy, B. H., Farley, K. A., and Zachos, J. C. (2010). An extraterrestrial 3 He-based timescale for the Paleocene–Eocene thermal maximum (PETM) from Walvis Ridge, IODP Site 1266. *Geochimica et Cosmochimica Acta* 74, 5098–5108. doi: 10.1016/j.gca.2010.03.039

Norris, R. D., and Röhl, U. (1999). Carbon cycling and chronology of climate warming during the Palaeocene/Eocene transition. *Nature* 401:775. doi: 10.1038/44545

Oldfield, F. (1991). Environmental magnetism—a personal perspective. *Quat. Sci. Rev.* 10, 73–85. doi: 10.1016/0277-3791(91)90031-O

Oliva-Urcia, B. (2004). *Geometría y cinemática rotacional en las Sierras Interiores y Zona Axial (sector de Bielsa) a partir del análisis estructural y paleomagnético*. Ph.D., Univeridad de Zaragoza.

Oliva-Urcia, B., and Pueyo, E. L. (2007). Rotational basement kinematics deduced from remagnetized cover rocks (Internal Sierras, southwestern Pyrenees). *Tectonics* 26, 67–99. doi: 10.1029/2006TC001955

Oliva-Urcia, B., Pueyo, E. L., and Larrasoaña, J. C. (2008). Magnetic reorientation induced by pressure solution: a potential mechanism for orogenic-scale remagnetizations. *Earth Planet. Sci. Lett.* 265, 525–534. doi: 10.1016/j.epsl.2007.10.032

Ortega, B., Caballero, M., Lozano, S., Vilaclara, G., and Rodríguez, A. (2006). Rock magnetic and geochemical proxies for iron mineral diagenesis in a tropical lake: Lago Verde, Los Tuxtlas, East-Central Mexico. *Earth Planet. Sci. Lett.* 250, 444–458. doi: 10.1016/j.epsl.2006.08.020

Orue-Etxebarria, X., Pujalte, V., Bernaola, G., Apellaniz, E., Baceta, J. I., Payros, A., et al. (2001). Did the Late Paleocene thermal maximum affect the evolution of larger foraminifers? Evidence from calcareous plankton of the Campo Section (Pyrenees, Spain). *Mar. Micropaleontol.* 41, 45–71. doi: 10.1016/S0377-8398(00)00052-9

Peters, C., and Dekkers, M. J. (2003). Selected room temperature magnetic parameters as a function of mineralogy, concentration and grain size. *Phys. Chem. Earth Parts A/B/C* 28, 659–667. doi: 10.1016/S1474-7065(03)00120-7

Plaziat, J.-C. (1981). Late Cretaceous to late Eocene palaeogeographic evolution of Southwest Europe. *Palaeogeogr. Palaeoclimatol. Palaeoecol.* 36, 263–320. doi: 10.1016/0031-0182(81)90110-3

Poblet, J., Muñoz, J. A., Travé, A., and Serra-Kiel, J. (1998). Quantifying the kinematics of detachment folds using three-dimensional geometry: application to the Mediano anticline (Pyrenees, Spain). *Geol. Soc. Am. Bull.* 110, 111–125. doi: 10.1130/0016-7606(1998)110<0111:QTKODF>2.3.CO;2

Puigdefàbregas, C., and Souquet, P. (1986). Tecto-sedimentary cycles and depositional sequences of the Mesozoic and Tertiary from the *Pyrenees.Tectonophysics* 129, 173–204. doi: 10.1016/0040-1951(86)90251-9

Pujalte, V., Orue-Etxebarria, X., Schmitz, B., Tosquella, J., Baceta, J. I., Payros, A., et al. (2003). "Basal Ilerdian (earliest Eocene) turnover of larger foraminifera: age constraints based on calcareous plankton and 13C isotopic profiles from new southern Pyrenean sections (Spain). Causes and consequences of globally warm climates in the early Paleogene," in *Geological Society of America Special Paper* (Geological Society of America), 205–221.

Pujalte, V., Robador, A., Payros, A., and Sams,ó, J. M. (2016). A siliciclastic braid delta within a lower Paleogene carbonate platform (Ordesa-Monte Perdido National Park, southern Pyrenees, Spain): record of the Paleocene–Eocene thermal maximum perturbation. *Palaeogeogr. Palaeoclimatol. Palaeoecol.* 459, 453–470. doi: 10.1016/j.palaeo.2016.07.029

Pujalte, V., Schmitz, B., Baceta, J. I., Orue-Etxebarria, X., Bernaola, G., Dinarès-Turell, J., et al. (2009). Correlation of the Thanetian-Ilerdian turnover of larger foraminifera and the Paleocene-Eocene thermal maximum: confirming evidence from the Campo area (Pyrenees, Spain). *Geol. Acta* 7, 161–175.

Ramón, M. J., Pueyo, E. L., Oliva-Urcia, B., and Larrasoaña, J. C. (2017). Virtual directions in paleomagnetism: A global and rapid approach to evaluate the NRM components. *Front. Earth Sci.* 5:8.

Ríos, L. M., Lanaja, J. M., and Frutos, E. (1982). *Hoja geológica y memoria n° 178 (Broto) del Mapa Geológico de España 1:50.000, 2ª ser.* (MAGNA), 60 pp. I.G.M.E.

Robador, A. (2008). *El Paleoceno e Ilerdiense inferior del Pirineo occidental: Estratigrafía y Sedimentología*. Ph.D., thesis University of the Basque Country, Spain. Publicaciones del Instituto Geológico y Minero de España, Serie Tesis Doctorales, 12, Madrid 312 pp.

Robador, A., Pujalte, V., Samsó, J. M., and Payros, A. (2009). Registro geológico del máximo térmico del Paleoceno-Eoceno en el Parque Nacional de Ordesa y Monte Perdido (Pirineo Central). *Geogaceta* 46, 111–114.

Robador, A., Sams,ó, J. M., Pujalte, V., Oliva, B., Gil, I., Soto, R., et al. (2010). "Cartografía geológica a escala 1: 25.000 del Parque nacional de Ordesa y Monte Perdido y su aplicación a la gestión e interpretación del medio natural del Parque Nacional," in *Proyectos de Investigación en Parques Nacionales 2006–2009,* (Madrid: Organismo Autónomo de Parques Nacionales Madrid), 7–28.

Rodríguez Méndez, L. (2011). *Análisis de la Estructura Varisca y Alpina en la Transversal Sallent*-Biescas. Pirineos centrales, Huesca.

Roest, W. R., and Srivastava, S. P. (1991). Kinematics of the plate boundaries between Eurasia, Iberia, and Africa in the North Atlantic from the Late Cretaceous to the present. *Geology* 19, 613–616.

Röhl, U., Norris, R. D., and Ogg, J. G. (2003). "Cyclostratigraphy of upper Paleocene and lower Eocene sediments at Blake Nose Site 1051 (western North Atlantic)," *Causes and Consequences of Globally Warm Climates in the Early Paleogene,* eds S. L. Wing, P. D. Gingerich, B. Schmitz, and E. Thomas (Boulder: Geological Society of America Special Paper), 576–589.

Röhl, U., Westerhold, T., Bralower, T. J., and Zachos, J. C. (2007). On the duration of the Paleocene-Eocene thermal maximum (PETM). *Geochem. Geophys. Geosyst.* 8:1784. doi: 10.1029/2007GC001784

Scheibner, C., and Speijer, R. P. (2009). Recalibration of the Tethyan shallow-benthic zonation across the Paleocene-Eocene boundary: the Egyptian record. *Geol. Acta.* 7, 195–214.

Scheibner, C., Speijer, R. P., and Marzouk, A. M. (2005). Turnover of larger foraminifera during the Paleocene-Eocene Thermal Maximum and paleoclimatic control on the evolution of platform ecosystems. *Geology* 33, 493–496. doi: 10.1130/G21237.1

Schmitz, B., and Pujalte, V. (2007). Abrupt increase in seasonal extreme precipitation at the Paleocene-Eocene boundary. *Geology* 35, 215–218. doi: 10.1130/G23261A.1

Schwartz,. E. J., and Vaughan,. D. J. (1972). Magnetic phase relations of pyrrhotite. *J. Geomagnetism Geoelect.* 24, 441–458.

Secord, R., Bloch, J. I., Chester, S. G., Boyer, D. M., Wood, A. R., Wing, S. L., et al. (2012). Evolution of the earliest horses driven by climate change in the Paleocene-Eocene Thermal Maximum. *Science* 335, 959–962. doi: 10.1126/science.1213859

Séguret, M. (1972). *Etude des Nappes et series décollées de la partie central du versant sud des Pyrénées – Caractère synsédimentaire, role de la compression et de la gravité.* USTELA, Montpellier.

Serra-Kiel, J., Hottinger, L., Caus, E., Drobne, K., Ferrandez, C., Jauhri, A. K., et al. (1998). Larger foraminiferal biostratigraphy of the Tethyan Paleocene and Eocene. *Bullet. Soc. Géol. France* 169, 281–299.

Teixell, A. (1992). *Estructura alpina en la transversal de la terminación occidental de la Zona Axial Pirenaica*. Tesis doctoral, Universitat de Barcelona.

Teixell, A. (1996). The Ansó transect of the southern Pyrenees: basement and cover thrust geometries. *J. Geol. Soc.* 153, 301–310. doi: 10.1144/gsjgs.153.2.0301

Thomas, E. (1990). Late Cretaceous through Neogene deep-sea benthic foraminifera (Maud Rise, Weddell Sea, Antarctica). *Proc. Ocean Drill. Prog. Sci. Res.* 113, 571–594.

Thomas, E., and Shackleton, N. (1996). "The Paleocene–Eocene benthic foraminiferal extinction and stable isotope anomalies," in *Correlation of the Early Paleogene in Northwest Europe. Geological Society Special Publication,* eds R. W. O. B. Knox, R. M. Corfield, and R. E. Dunay (The Geological Society Publishing House Unit Brassmill Enterprise Centre Brassmill), 401–441.

Trindade, R. I. F., Mintsa Mi Nguema, T., and Bouchez, J. L. (2001). Thermally enhanced mimetic fabric of magnetite in a biotite granite. *Geophys. Res. Lett.* 28, 2687–2690. doi: 10.1029/2001GL013218

Van de Velde, E. (1967). Geology of the Ordesa overthurst mass, Spanish Pyrenees, province of Huesca. *Estudios Geol.* 26, 163–201.

Van Lunsen, H. A. (1970). *Geology of the Ara-Cinca region, Spanish Pyrenees, province of Huesca: (with special reference to compartmentation of the Flysch basin)*. Doctoral dissertation, Utrecht University.

Vergés, J., Fernàndez, M., and Martínez, A. (2002). The Pyrenean orogen: pre-, syn-, and post-collisional evolution. *J. Virt. Expl.* 8, 55–74. doi: 10.3809/jvirtex.2002.00058

Villasante-Marcos, V., Hollis, C. J., Dickens, G. R., and Nicolo, M. J. (2009). Rock magnetic properties across the Paleocene-Eocene thermal maximum in Marlborough, New Zealand. *Geol. Acta* 7, 229–242. doi: 10.1344/105.000000280

Wang, Y., Dong, H., Li, G., Zhang, W., Oguchi, T., Bao, M., et al. (2010). Magnetic properties of muddy sediments on the northeastern continental shelves of China: implication for provenance and transportation. *Mar. Geol.* 274, 107–119. doi: 10.1016/j.margeo.2010.03.009

Wing, S. L., Harrington, G. J., Smith, F. A., Bloch, J. I., Boyer, D. M., and Freeman, K. H. (2005). Transient floral change and rapid global warming at the Paleocene-Eocene boundary. *Science* 310, 993–996. doi: 10.1126/science.1116913

Zachos, J. C., Dickens, G. R., and Zeebe, R. E. (2008). An early Cenozoic perspective on greenhouse warming and carbon-cycle dynamics. *Nature* 451:279. doi: 10.1038/nature06588

Zamagni, J., Mutti, M., Ballato, P., and Košir, A. (2012). The Paleocene–Eocene thermal maximum (PETM) in shallow-marine successions of the Adriatic carbonate platform (SW Slovenia). *Bulletin* 124, 1071–1086. doi: 10.1130/B30553.1

Zeebe, R. E. (2013), What caused the long duration of the Paleocene-eocene thermal maximum? *Paleoceanography* 28, 440–452, doi: 10.1002/palo.20039

Conflict of Interest Statement: The authors declare that the research was conducted in the absence of any commercial or financial relationships that could be construed as a potential conflict of interest.